

Virtual Synchronous Machine Control with Adaptive Inertia Applicable to an MMC Terminal

Ana Julieth Marin Hurtado

This thesis presented as a partial requirement for the degree of:

Master's in Electrical Engineering

Main advisor:

Andrés Escobar Mejía, Ph.D.

Second Advisor:

Walter Julián Gil, Ph.D.

**Universidad Tecnológica de Pereira
Electrical Engineer Master Program
Pereira, Colombia
2020**

Virtual Synchronous Machine Control with Adaptive Inertia Applicable to an MMC Terminal

Ana Julieth Marín Hurtado

**Universidad Tecnológica de Pereira
Electrical Engineer Master Program
Pereira, Colombia**

2020

ABSTRACT

Renewable energy sources (RES) penetration levels are increasing in the power grid. However, it does not have inertia as a traditional synchronous generator, causing a reduction in the inertia and damping in the power grid, impacting the stability during power changes in the grid, causing large frequency deviations. The virtual synchronous machine (VSM) concept has become an attractive solution to emulate the synchronous machine characteristics and supply the inertia and damping property in the system. It consists of emulating the synchronous machine's static and dynamic properties by power electronic converters and energy storage systems. Nevertheless, the implementation and design of the VSM is a challenge since it must be flexible in the presence of load fluctuations, preventing the oscillations and frequency overshoot from increasing during system disturbances. Hence, the VSM with adaptive inertia has become a potential solution because it provides the inertia and damping factor to the grid according to the load variations and different RES penetration levels in the system. Therefore, the inertia estimation is necessary to use the special techniques that guarantee the balance between the power and frequency response.

This thesis proposes a proportional-integral (PI), linear quadratic regulator (LQR), and model predictive control (MPC) to estimate the inertia of the VSM controller. Since the PI controller solves the balance problem between the power and frequency responses. Therefore, it uses a control law based on the cross error of the power change and the frequency droop in the system. The LQR solves the optimization problem between the power and frequency responses, accomplishing a fast response and small oscillations. The MPC solves the balance problem between the power and frequency response, determining an optimal trajectory of outputs with minimal cost of the input signals (inertia and damping factor). These controllers solve the balance problem between the power and frequency responses, fast response, and small oscillations. A comparison with a VSM with constant inertia is performed to validate the proposed method. For this purpose, a 200 MW/200 kV modular multilevel (MMC) terminal (commonly used to connect offshore wind farms with the power grid), with seven sub-modules, is used as a power converter.

Time-domain simulations have been carried out in the MMC terminal, considering variations in the active and reactive powers to show the power and frequency responses using both controllers. Results show that the VSM-MPC controller presents lower frequency

oscillations, minimum and maximum frequency, settling time, and rate of change of frequency (ROCOF) compared to the traditional approach and other controllers.

TABLE OF CONTENTS

CHAPTER 1.	INTRODUCTION.....	9
CHAPTER 2.	MODULAR MULTILEVEL CONVERTER	12
2.1	General Principles.....	12
2.2	Operating Principle	12
2.3	Equivalent Circuit	13
2.4	Modulation Strategies in the MMC	15
2.4.1	CD-PWM.....	16
2.4.2	CPS-PWM	16
2.5	The Control Applied to the MMC	18
2.5.1	Average Voltage Control.....	18
2.5.2	Individual Voltage Control.....	19
2.6	The reference signal	19
CHAPTER 3.	SYNCHRONOUS MACHINE	21
3.1	Basic Concepts.....	21
3.2	Synchronous Machine Model	21
3.2.1	Electrical part.....	22
3.2.2	The Swing Equation	24
CHAPTER 4.	VIRTUAL SYNCHRONOUS MACHINE.....	26
4.1	Basic Concepts.....	26
4.2	Frequency Drooping	28
4.3	Voltage Drooping	29
CHAPTER 5.	ADAPTIVE INERTIA FOR A VIRTUAL SYNCHRONOUS MACHINE APPLICABLE TO A MODULAR MULTILEVEL CONVERTER.....	32
5.1	Linear Model for Inertia Estimation	32
5.2	Adaptive Inertia using a PI Controller	33
5.3	Adaptive Inertia using Linear Quadratic Regulator (LQR) Controller.....	33
5.4	Adaptive Inertia using Model Predictive Control (MPC) Controller	35
CHAPTER 6.	SIMULATIONS AND RESULTS.....	38
6.1	The MMC output active power.....	39
6.2	The MMC output reactive power.....	41
6.3	VSM dynamic frequency response	44

6.4	Analysis of the results.....	45
CHAPTER 7.	CONCLUSIONS.....	48
REFERENCES	50

LIST OF FIGURES

Fig. 2.1. Modular Multilevel Converter.	13
Fig. 2.2. The MMC per-phase equivalent circuit.	14
Fig. 2.3. Carrying signal CD-PWM with method PD (a), POD (b), and APOD (c).	16
Fig. 2.4. The carrying and reference signal for CPS-PWM	17
Fig. 2.5. PWM for <i>SM1</i> (a), <i>SM2</i> (b), <i>SM3</i> (c), <i>SM4</i> (d), <i>SM5</i> (e), <i>SM6</i> (f).....	18
Fig. 2.6. Average Voltage control scheme.	18
Fig. 2.7. Individual voltage control in the capacitors.	19
Fig. 2.8. Upper (a) and lower (b) arms voltage reference generation	20
Fig. 3.1. Schematic of three-phase synchronous machine with a cylindrical rotor [57].	23
Fig. 4.1. Virtual synchronous machine.....	27
Fig. 4.2. The $P - \omega$ droop control scheme.....	29
Fig. 4.3. The $Q - v$ droop control scheme.	31
Fig. 5.1. The VSM-PI controller scheme.....	33
Fig. 5.2. The VSM-LQR controller schematic.	34
Fig. 6.1. MMC controller schematic.	38
Fig. 6.2. Comparison of the output active power of the MMC with the power estimated by the VSM controller.	40
Fig. 6.3. Comparison of the output active power of the MMC with the power estimated by the VSM-PI (a), VSM-LQR (b) and VSM-MPC (c) controllers.....	41
Fig. 6.4. Comparison of the output reactive power of the MMC with the power estimated by the VSM controller.	42
Fig. 6.5. Comparison of the output reactive power of the MMC with the power estimated by the VSM-PI (a), VSM-LQR (b) and VSM-MPC (c) controllers.....	43
Fig. 6.6. The frequency of the VSM with constant inertia.	44
Fig. 6.7. The VSM frequency with the estimated inertia using PI (a),.....	45
Fig. 6.8. The frequency error.....	47

LIST OF TABLE

Table 2.1 Submodule Switching States [46].	13
Table 6.1. System Parameters	39
Table 6.2. Linear System: Initial Conditions.....	39
Table 6.3. The results summary.....	46

CHAPTER 1. INTRODUCTION

The generation of electricity in power systems is performed by synchronous generators that work with speed governors and voltage regulators that control both system frequency and output voltage [1], [2]. The rotating mass of the generators provides the inertia and the required damping, injecting or absorbing kinetic energy to the system to mitigate frequency fluctuations and counteract the effect of the rate of change of frequency (ROCOF) during disturbances [3]. However, the rotating inertia has been decreasing in the grid due to the increase in the penetration levels of the renewable energy sources (RES) [4]. In 2017, 19.3% of the world's energy was produced by RES, where 10.2 % correspond to geothermal, solar, and wind power, and 9.1 % due to biomass [2], [5].

In Colombia, 69.92% of the electricity is based on hydroelectric plants, which provide high inertia levels; 0.1% is based on solar energy, and 0.1% is based on wind energy [6]. Nevertheless, according to la Unidad de Planeación Minero Energética (UPME), the RES will increase by up to 13.8% by 2031 [2], [6]. Yet, RESs are fluctuating and unpredictable and causes the energy supply variable [7]. The use of solar and wind energy in power systems demand the implementation of power electronic converters, advanced control algorithms, filters, etc., which keep variables within permitted thresholds [8]. On the other hand, RES has small, or none, rotating mass to provide damping, which affects frequency stability during disturbances and produces large frequency deviations [9]. This could lead to events such as load-shedding and large-scale blackouts [2], [10], [11].

The concept of virtual synchronous machine (VSM) has been studied to overcome the issues mentioned above. It consists of a power converter, which are strategically controlled, emulating an inertia that injects/absorbs active power to/from the grid [12]. The VSM emulates the primary frequency and the voltage regulation function of the synchronous generators through the droop control.

The VSM simulates the rotor swing characteristics of the synchronous generator, and providing –or mimic– virtual inertia and ancillary services, as synchronous generators do [2], [13], [14]. However, the design and implementation of the VSM have difficulties such as the correct selection of the inertia, damping –for stable operation of VSM–, and control in the presence of load fluctuations [2]. The selection of virtual inertia values has been investigated

in the literature [10], [15]–[18], and it has been calculated depending on the penetration levels of RES [13]. The selection of this inertia is based on the system dynamic performance. For this purpose, an extensive eigenvalues analysis is required [13]. Incorrect sensitivity analysis may cause an incorrect selection of the inertia and damping factor, which are used to emulate the VSM. This causes undesired frequency transients and power oscillations under load variations, affecting the stability and performance of the system under different penetration levels of RES [2], [14]. As an advantage, the VSM's inertia and damping parameters can be variable and adjustable during load changes and different RES penetration levels. This leads to a VSM with adequate and fast response [13].

In the specialized literature, several investigations to design and implement the VSM have been reported [10]–[26]. However, the inertia estimation in the VSM is not a straightforward task because it is challenging to adapt control strategies to real-time system conditions [27]. Despite this, in [28], a VSM with a self-adaptive inertia algorithm was proposed to reduce power oscillations. However, a damping factor analysis was not presented. In [29], a self-tuning virtual VSM was introduced to search optimal constant inertia and damping factor continuously, but its implementation was complicated and no carry-out damping factor analysis [2]. In [30], an adaptive control strategy based on “ping pong” control was proposed, to change the inertia between upper and lower values. However, the principle of selecting two values was not given in the literature [2].

In [31], an adaptive inertia strategy was proposed based on the power angle curve of a synchronous generator. The virtual inertia was selected to meet the requirements of power variations. However, choosing the initial value of inertia and the damping factor at a steady-state was not reported [2]. In the above-mentioned works, the presented control techniques to estimate the inertia was insufficient and unstable under high RES penetration. Other techniques in [32]–[35] was developed as fuzzy logic, artificial neural network, and optimal control. Nevertheless, these approaches had some limitations under load variations, such as the inertia estimation, high computational burden, and control complexity. In some of these controllers, the Bang-Bang technique was considered, which consists of switching inertias between a threshold band (large and small inertia constant); however, each switching cause power oscillations [2], [22].

This thesis presents several adaptive inertia control schemes for VSM, applicable to an MMC. The controllers used to obtain the adaptive inertia for VSM are Proportional-Integral (PI) control, Linear Quadratic Regulator (LQR) control, and Model Predictive Control (MPC). In the first case, the adaptive inertia is calculated as the difference between the reference frequency, times the output active power, and the reference active power times the frequency estimated by the VSM. The LQR and MPC control objective is to calculate the inertia and damping constants, guaranteeing the balance between the fast frequency response and the frequency oscillations in the power system disturbances presence.

The adaptive inertia control schemes for VSM proposed in this thesis acting on a 200 kV/200 MW MMC inverter, with seven submodules per arm. The MMC control is divided into the average voltage control, the individual voltage capacitor control, and the active and reactive power control. The VSM is responsible for active and reactive control. In time-domain simulations, the active and reactive power changes in the MMC are considered to show the performance of the VSM with adaptive inertia, estimating with proportional-integral (PI), linear quadratic regulator (LQR), and model predictive control (MPC).

This thesis is organized as follows: fundamentals, operating principles, and the MMC model used to emulate the VSM are presented in CHAPTER 2. The synchronous machine model used to design the VSM is introduced in CHAPTER 3. The basic description of the VSM concepts and the frequency and voltage drooping is presented in CHAPTER 4. The control schemes (PI, LQR, and MPC) used to estimate the inertia for the VSM with adaptive inertia are explained in CHAPTER 5. The test system and the VSM with adaptive inertia results are presented in CHAPTER 6. This chapter compares the virtual frequency, active and reactive power signals with the different control schemes. Finally, conclusions and remarks are given in CHAPTER 7.

CHAPTER 2. MODULAR MULTILEVEL CONVERTER

2.1 General Principles

Modular Multilevel Converters (MMC) receive considerable attention for high-voltage and high-power applications such as high-voltage direct current (HVDC) transmission system and the integration of –for instance– renewable energy sources, hydro-power plants, etc. Which are located far from demand centers [36], [37]. The study and number of applications of MMC have increased due to their well-known advantages (e.g., modularity, reduced voltage stress across power devices, low switching losses, asymmetric operation capability, better output performance, and reduce the size of output filters) over conventional topologies, such as the traditional VSC-HVDC [37]–[40].

The operating principle of the MMC requires special attention due to its inherent structure. In this sense, advanced modulation techniques are implemented to keep both the voltage balance and the circulating currents below the reference values in each arm [41]–[44]. The latest one causes second-order harmonics that may cause capacitors voltage imbalances, efficiency reduction, power devices lifetime decrease, output current distortion, and oversize of passive components; furthermore, it may cause instability during transients unless controlled [45].

2.2 Operating Principle

Fig. 2.1 presents a traditional bidirectional MMC terminal, where two arms (upper and lower) form a phase. Each arm consists of N -series submodules (SM) and an inductance (L_{arm}) in series to limit the current due to voltage mismatch between the SM. Each upper arm is connected between the positive bus and the midpoint phase of the converter. Each lower arm is connected between the negative bus and the midpoint phase; thus, the dc voltage (V_{dc}) is divided by two.

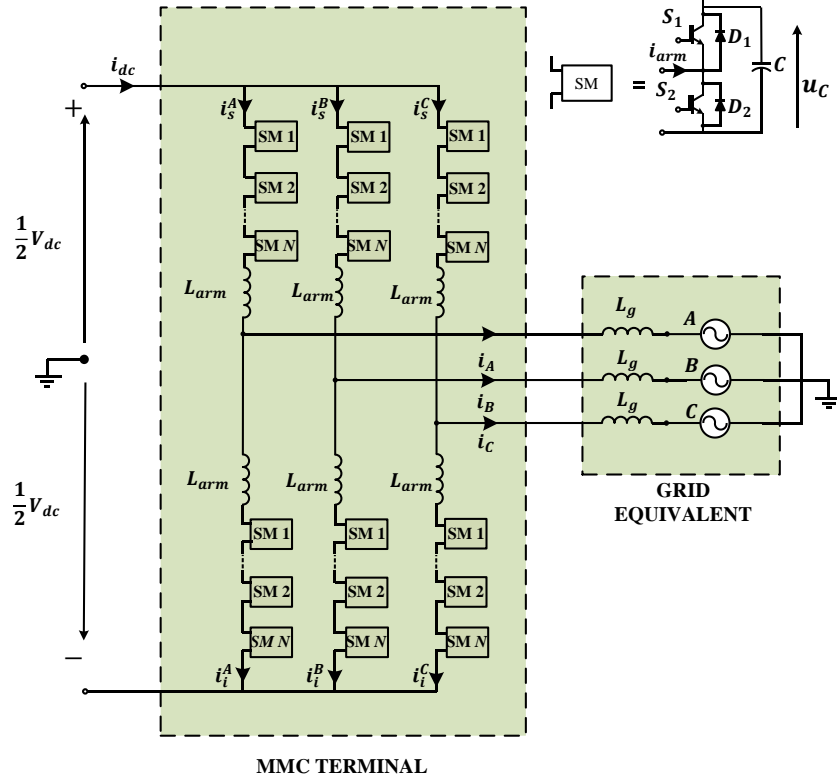


Fig. 2.1. Modular Multilevel Converter.

Each MMC submodule is either in a full-bridge or half-bridge configuration. The half-bridge type is shown in Fig. 2.1 (top right), which consists of two IGBTs S_1 and S_2 and a parallel capacitor C . The possible switching states in each submodule are shown in Table 2.1.

2.3 Equivalent Circuit

A three-phase balanced system connected to the MMC terminal is considered for analysis [47]. The MMC per-phase equivalent circuit connected to a resistive load R_o is presented in Fig. 2.2.

TABLE 2.1 SUBMODULE SWITCHING STATES [46].

S_1	S_2	D_1	D_2	Current Direction	Capacitor State	Output Voltage
OFF	ON	OFF	OFF	$i_{arm} > 0$	Unchanged	0
OFF	OFF	OFF	ON	$i_{arm} < 0$	Unchanged	0
OFF	OFF	ON	OFF	$i_{arm} > 0$	Charging	u_c
ON	OFF	OFF	OFF	$i_{arm} < 0$	Discharging	u_c

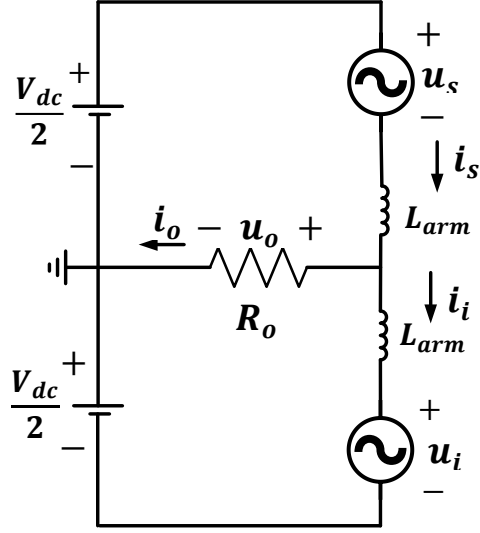


Fig. 2.2. The MMC per-phase equivalent circuit.

The SMs are considered as two voltage sources, where u_s and u_i are the submodules output voltage of the upper and lower arm, respectively; i_s and i_i are the upper and lower arm currents, respectively; u_o and i_o are the output leg voltage and current, respectively.

Based on the circuit in Fig. 2.2 and applying Kirchhoff second law, it is possible to get:

$$\begin{aligned} \frac{V_{dc}}{2} - u_s - L_{arm} \frac{di_s}{dt} - u_o &= 0 \\ \frac{V_{dc}}{2} - u_i - L_{arm} \frac{di_i}{dt} + u_o &= 0 \end{aligned} \quad (2.1)$$

Applying the Kirchhoff first law in Fig. 2.2 is possible to get:

$$i_s - i_i - i_o = 0 \quad (2.2)$$

From (2.2), it is possible to get:

$$\begin{aligned} i_s &= i_i + i_o \\ i_i &= i_s - i_o \end{aligned} \quad (2.3)$$

By taking current measurements at the MMC terminal, the differential current is obtained in the function of i_s and i_i in the following way:

$$i_{diff} = \frac{i_s + i_i}{2} \quad (2.4)$$

From (2.4), it is possible to get:

$$\begin{aligned} i_s &= 2i_{diff} - i_i \\ i_i &= 2i_{diff} - i_s \end{aligned} \quad (2.5)$$

Replacing (2.5) in (2.3), it is possible to get:

$$\begin{aligned} i_s &= i_{diff} + \frac{i_o}{2} \\ i_i &= i_{diff} - \frac{i_o}{2} \end{aligned} \quad (2.6)$$

From (2.1) and (2.6), it is possible to get:

$$\begin{aligned} u_s &= \frac{V_{dc}}{2} - \frac{L_{arm}}{2} \frac{di_{diff}}{dt} - \left(\frac{L_{arm}}{4} \frac{di_o}{dt} + u_o \right) = 0 \\ u_i &= \frac{V_{dc}}{2} - \frac{L_{arm}}{2} \frac{di_{diff}}{dt} + \left(\frac{L_{arm}}{4} \frac{di_o}{dt} + u_o \right) = 0 \end{aligned} \quad (2.7)$$

Defining the electromotive force generated by the MMC as:

$$e_o = \frac{L_{arm}}{4} \frac{di_o}{dt} + u_o \quad (2.8)$$

And the inductor voltage due to the difference current is

$$v_m = \frac{L_{arm}}{2} \frac{di_{diff}}{dt} \quad (2.9)$$

Finally, replacing (2.8) and (2.9) in (2.7) is possible to get:

$$\begin{aligned} u_s &= \frac{V_{dc}}{2} - v_m - e_o \\ u_i &= \frac{V_{dc}}{2} - v_m + e_o \end{aligned} \quad (2.10)$$

In (2.10), the relationship between the electromotive force and the upper and lower voltage of MMC is observed. The electromotive force is generated from the virtual synchronous machine is explained in CHAPTER 4.

2.4 Modulation Strategies in the MMC

This section studies different modulation strategies used in the MMC to generate the gate signal for the SM's semiconductor devices. Based on this, the VSM control scheme is presented in this thesis, using the Carrier Phase Shifted modulation technique for the MMC. The modulation methods have been studied in the literature is Nearest Level Modulation (NLM), Space Vector Modulation (SVPWM), Sinusoidal PWM (SPWM), and Pulse Width Modulation (PWM). However, the NLM and SVPWM techniques, as MMC levels increase to require a high computational burden [48], [49].

The PWM technique consists of the logic comparison between a reference signal (sine wave) and a carrying signal (triangular wave). When the magnitude of the reference signal is

higher than the carrying signal, a logic “1” is generated at the comparator’s output. For the modulation case to the MMC devices, the carrying number is equal to N (equal to submodules number per arm in the MMC). The PWM techniques proposed for the MMC are Carrier-Disposition PWM (CD-PWM) y Carrier Phase Shifted (CPS-PWM).

2.4.1 CD-PWM

The CD-PWM requires N identical triangular signals in magnitude and frequency, shifting in the abscissa axis. Each signal is compared with the sine reference signal. The triangular signal layout is variable, and it is classified into Phase Disposition (PD), Phase Opposition Disposition (POD), and Alternate Phase Opposition Disposition (APOD). The different signals layout is shown in Fig. 2.3.

2.4.2 CPS-PWM

The CPS-PWM requires N identical triangular signals in magnitude and frequency; each signal is compared with the sine reference signal. With a phase shift of:

$$\alpha = \frac{360^\circ}{N} \quad (2.8)$$

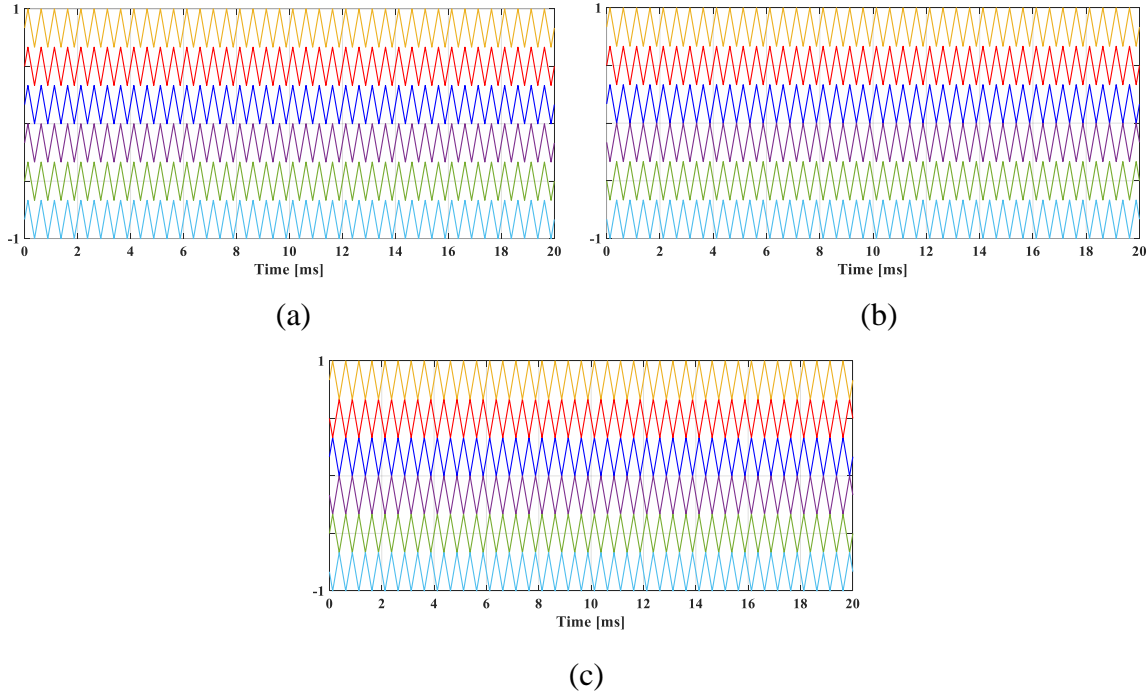


Fig. 2.3. Carrying signal CD-PWM with method PD (a), POD (b), and APOD (c).

Fig. 2.4 shows the carrying signals and reference signal of a terminal with $N=6$ and switching frequency equal to 2000 Hz. The PWM is obtained as of CPS-PWM is presented in Fig. 2.5.

The disadvantages of using the CD-PWM modulation technique are the uneven voltage ripple distribution through the sub-module capacitors, which affects the ac side voltages harmonic distortion and large circulating current magnitude [39]. Therefore, the modulation strategy used in the proposed control scheme in this thesis is CPS-PWM.

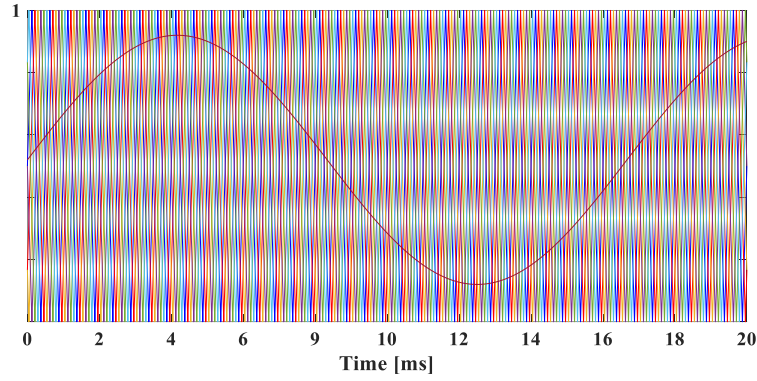
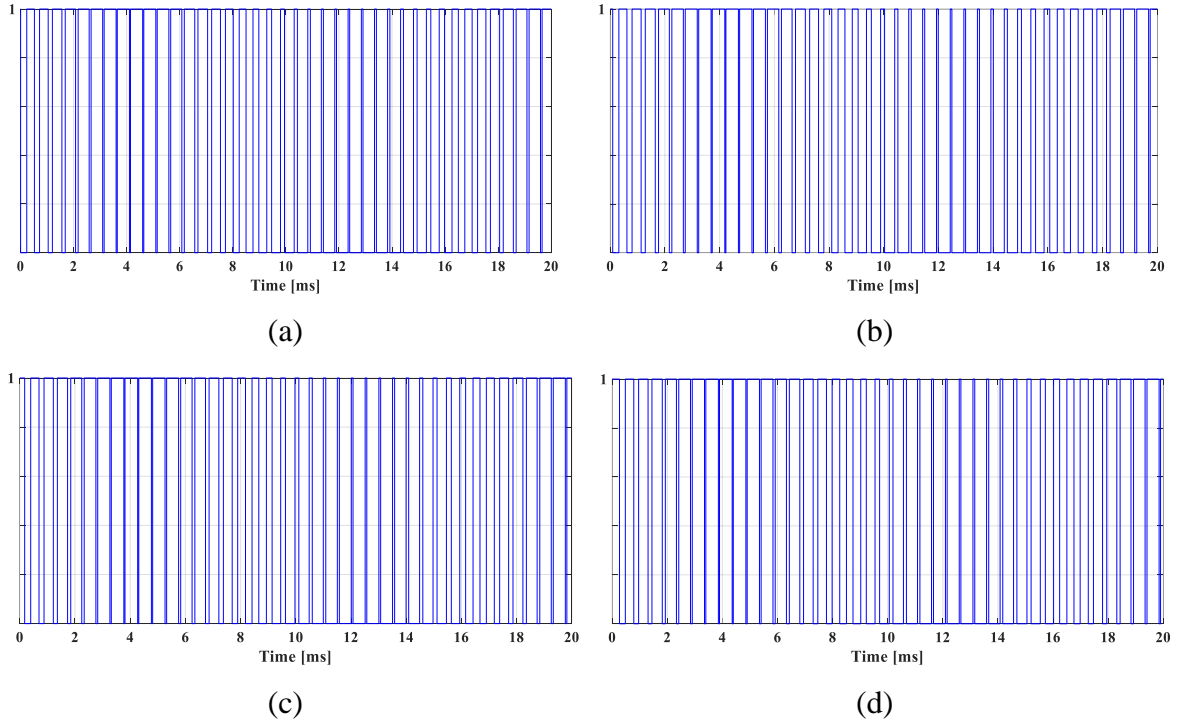


Fig. 2.4. The carrying and reference signal for CPS-PWM



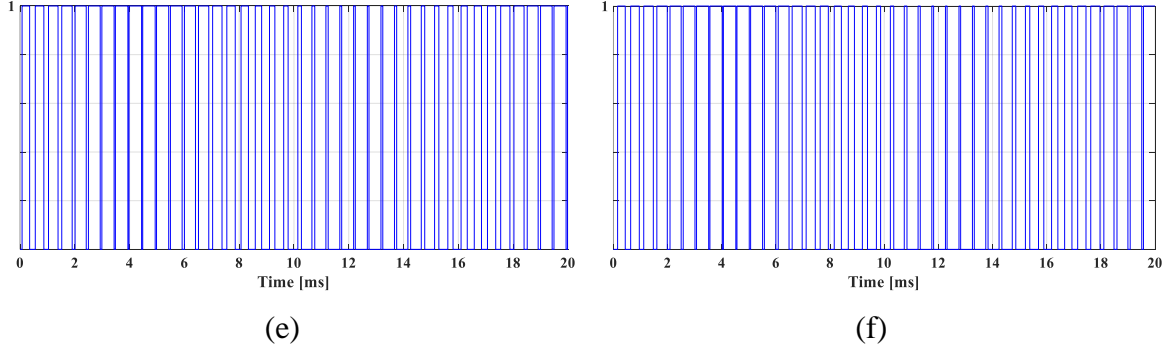


Fig. 2.5. PWM for SM_1 (a), SM_2 (b), SM_3 (c), SM_4 (d), SM_5 (e), SM_6 (f).

2.5 The Control Applied to the MMC

The MMC control is composed of the active and reactive power controllers, the individual voltage control of capacitors, and the average voltage control. The MMC control based on the synchronous machine model for powers is developed in CHAPTER 3. The individual voltage control and the average voltage control are given based on [50], as shown following:

2.5.1 Average Voltage Control

In order to reduce the capacitor's voltage ripple, the control scheme presented in Fig. 2.6. is used [51]–[53]. The voltage that each capacitor withstand in the SM is V_{dc}/N , therefore, it is taken as the average reference value:

$$v_{c_M}^* = \frac{V_{dc}}{N} \quad (2.10)$$

where $\overline{v_{c_M}}$ is the average capacitor voltage, and $v_{c_M}^*$ is the average capacitor voltage reference, $v_{m_M}^*$ is the command voltage, which is used in the voltage reference generation for PWM, and $M \in a, b, c$.

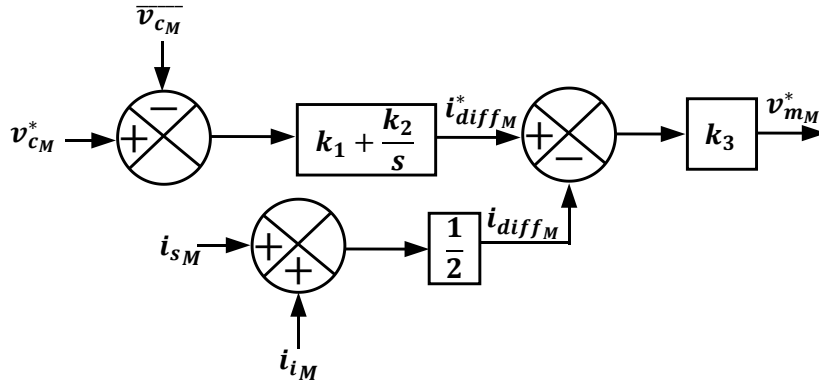


Fig. 2.6. Average Voltage control scheme.

The average voltage per phase is defined as:

$$\overline{v_{cM}} = \frac{1}{2N} \sum_{j=1}^{2N} v_{cj} \quad (2.11)$$

The reference circulating current is described as:

$$i_{diffM}^* = k_1(v_c^* - \overline{v_c}) + \frac{k_2}{s}(v_c^* - \overline{v_c}), \quad (2.12)$$

The output control for average voltage control v_m^* is described by:

$$v_{mM}^* = k_3(i_{circ}^* - i_{circM}) \quad (2.13)$$

where k_1 y k_3 are proportional constants, and k_2 is integral constant, the sub-index $M \in A, B, C$.

2.5.2 Individual Voltage Control

The individual voltage is responsible for control the capacitor voltage value to each SM. The magnitude voltage reference is given by (2.10), and the current polarities i_{sM} and i_{iM} provide the control signal [52], as shown in Fig. 2.7.

where v_{cujM} is the voltage measurement of each capacitor.

The section 2.5 are generated the voltages references v_{mM}^* and v_{yjM} for the upper and lower arms voltage reference generation as shown in section 2.6, which are used to CPS-PWM in MMC.

2.6 The reference signal

Once the active and reactive powers control, individual voltages control, and average voltage control have been developed, the reference signal for upper and lower arms necessary for the CPS-PWM is produced, as shown in Fig. 2.8. The voltage reference signals for upper u_{sM}^* and lower u_{iM}^* arms are 180° offset from each other.

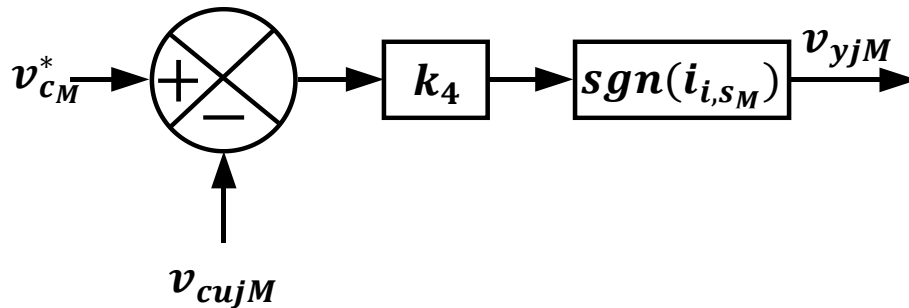
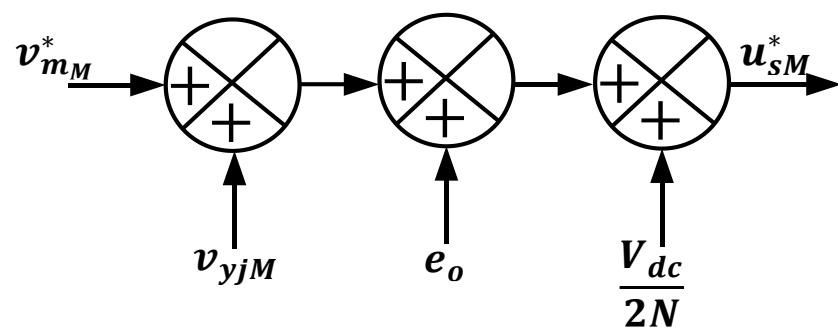
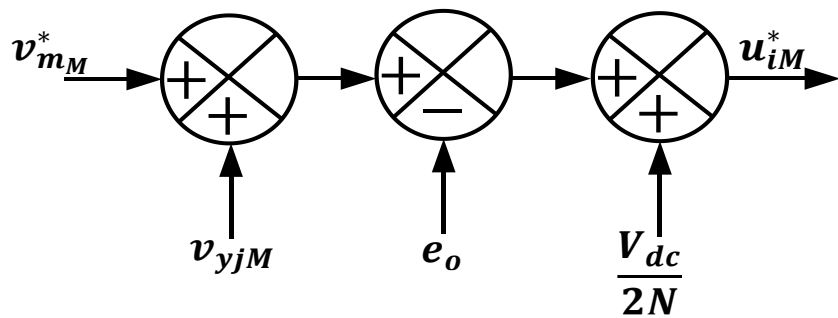


Fig. 2.7. Individual voltage control in the capacitors.



(a)



(b)

Fig. 2.8. Upper (a) and lower (b) arms voltage reference generation

CHAPTER 3. SYNCHRONOUS MACHINE

3.1 Basic Concepts

A synchronous machine is an ac machine, where the speed of the rotating magnetic field (n_s), is the shaft speed. The frequency of the induced armature's voltages (f_e) is given by:

$$f_e = \frac{n_s P}{120}, \quad (3.1)$$

where P is the number of poles of the machine.

The machine parts are the stator and rotor. The stator is the stationary part where the induced windings are located, while the rotor is the moving part, where the inductor windings (field windings) and damping windings are located. The inductor winding creates the magnetic field, thanks to the action of dc currents flowing through it.

According to the rotor type, there are two types of synchronous machines: the salient pole rotor and the non-salient (cylindrical) rotor. The salient rotor is used in multipolar machines that rotate at low speeds (hydroelectric plants). The non-salient rotor (with two and four poles) rotates at high speed and is usually used in thermal power plants. [54].

The synchronous generator is 90 % of power generators in conventional power plants due to which have dynamic proprieties allows improving the grid stability, as [15]:

- The synchronous generator provides the possibility of adjusting active output power due to the dependency of the grid frequency of the rotor speed.
- The generator excitation current change can regulate the output voltage.
- Short-term energy supply due to the inertia.
- Stable parallel operation with other generators.
- Load sharing can be achieved by applying a frequency-active power-static, according to grid frequency.

The above dynamic properties of synchronous generators will be reproduced from the converters used as an interface for the renewable energies connection, as shown in section 4.1. To improve the stability of the system before the high penetration of these energies.

3.2 Synchronous Machine Model

For the analysis, some assumptions are made to get the machine model [55]: phases have sinusoidal current and voltage waveforms, $P=2$. The machine rotor is a non-salient type rotor,

and thus all the stator inductances are constant [56], the action of the damping windings is negligible. Furthermore, there is no saturation effect on the core, and the Foucault currents are insignificant.

The synchronous machine model is divided in two parts: The electrical part and the mechanical part.

3.2.1 Electrical part

The cross-section of a three-phase synchronous machine with a non-salient rotor is presented in Fig. 3.1 [57].

where aa' , bb' , cc' represent the per-phase distributed windings of the stator, that produce the sinusoidal MMF, ff' represents the field winding. Dots and crosses indicate the current direction.

The flux linkages of the armature Φ_a , Φ_b , Φ_c and field windings Φ_f are:

$$\begin{aligned} \Phi_a &= L_{aa}i_a + L_{ab}i_b + L_{ac}i_c + L_{af}i_f & \Phi_c &= L_{ca}i_a + L_{cb}i_b + L_{cc}i_c + L_{cf}i_f \\ \Phi_b &= L_{ba}i_a + L_{bb}i_b + L_{bc}i_c + L_{bf}i_f & \Phi_f &= L_{af}i_a + L_{bf}i_b + L_{cf}i_c + L_{ff}i_f \end{aligned} \quad (3.3)$$

where L_{aa} , L_{bb} , L_{cc} are the stator self-inductances that produce the sinusoidal MMF, L_{ab} , L_{bc} , L_{ac} are the mutual inductances between each phase windings, L_{ff} is a field self-inductance, L_{af} , L_{bf} , L_{cf} are the mutual inductances between the stator windings and field winding, i_a , i_b , i_c are the stator phase currents and i_f is the field current in the rotor. Hence,

$$\mathbf{\Phi} = \begin{bmatrix} \Phi_a \\ \Phi_b \\ \Phi_c \end{bmatrix} \quad \mathbf{i} = \begin{bmatrix} i_a \\ i_b \\ i_c \end{bmatrix} \quad \mathbf{cos} \theta = \begin{bmatrix} \cos \theta \\ \cos(\theta - \frac{2\pi}{3}) \\ \cos(\theta - \frac{4\pi}{3}) \end{bmatrix} \quad \mathbf{sin} \theta = \begin{bmatrix} \sin \theta \\ \sin(\theta - \frac{2\pi}{3}) \\ \sin(\theta - \frac{4\pi}{3}) \end{bmatrix} \quad (3.4)$$

The mutual inductances are in function of the rotor angle θ as follows [58]:

$$\begin{aligned} L_{af} &= M_f \cos \theta \\ L_{bf} &= M_f \cos(\theta - \frac{2\pi}{3}) \\ L_{cf} &= M_f \cos(\theta - \frac{4\pi}{3}) \end{aligned} \quad (3.2)$$

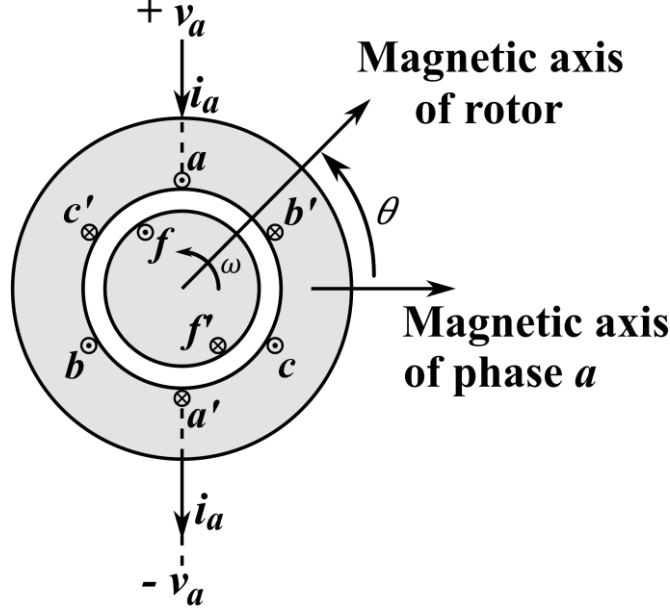


Fig. 3.1. Schematic of three-phase synchronous machine with a cylindrical rotor [57].

where M_f is the mutual inductance between the field coil and the stator coil, with $M_f > 0$. Therefore, the flux linkages can be written as:

$$\Phi = L_s \mathbf{i} + M_f i_f \cos \theta \quad (3.5)$$

where $L_s = L_{ii} + L_{ij}$, the subscripts i and j represent each phase (a, b, c). The flux linkage of the field is:

$$\Phi_f = L_{ff} i_f + M_f \langle \mathbf{i}, \cos \theta \rangle \quad (3.6)$$

where $\langle ., . \rangle$ is the inner product between two vectors. $M_f \langle \mathbf{i}, \cos \theta \rangle$ is constant if the three-phase currents are sinusoidal and balanced.

The terminal voltage of the synchronous machine $\mathbf{v} = [v_a \ v_b \ v_c]^T$ are:

$$\mathbf{v} = -R_s \mathbf{i} - \frac{d\Phi}{dt} = -R_s \mathbf{i} - L_s \frac{d\mathbf{i}}{dt} + \mathbf{e}_o \quad (3.7)$$

where L_s is the armature inductance, R_s is the armature resistance, and $\mathbf{e}_o = [e_{oa} \ e_{ob} \ e_{oc}]^T$ is the induced voltage vector due to the action of the field winding, which is:

$$\mathbf{e}_o = M_f i_f \dot{\theta} \sin \theta \quad (3.8)$$

The electromotive force is generated by (3.8) to use for the voltage reference signal generation for the CPS-PWM, as shown in Fig. 2.8.

3.2.2 The Swing Equation

For the study of the machine oscillation equation and the rate of the rotor speed change, it is assumed that the machine shaft is solid with inertia constant M , considering the machine rotor as rotating free-body [58]. The machine oscillation equation describes the imbalance effect between electromagnetic torque and mechanic torque [54], causing the acceleration or deceleration of the shaft. However, the rotor presents a portion of stored kinetic energy, which is beneficial in the torques imbalances case in the rotor [59]. The kinetic energy will be absorbed by the system to reduce the machine speed and the frequency deviations [59]. The net torque in N.m when the machine has an unbalance between its set torques is:

$$T_a = T_m - T_e \quad (3.9)$$

where T_a is the acceleration torque, T_m is the mechanical torque and T_e is the electromagnetic torque. The equation (3.9) is implemented for the synchronous machine operating as a generator and motor.

The acceleration torque is defined as the inertia times the acceleration of the shaft; therefore, (3.9) can be written as:

$$M \frac{d\omega_m}{dt} = T_m - T_e \quad (3.10)$$

where, ω_m is the rotor angular speed in rad/s, M is the combined moment inertia of the generator and turbine in kg.m² ω_m is the rotor angular speed in rad/s and t is the time in s. The inertia constant in per unit is defined as the kinetic energy in W.s to the nominal velocity divided by the VA base, as shown following [54]:

$$H = \frac{M\omega_{m0}^2}{2VA_{base}} \quad (3.11)$$

where ω_{m0} is the nominal angular speed. The inertia moment based on the inertia constant is:

$$M = \frac{2H}{\omega_{m0}^2} VA_{base} \quad (3.12)$$

The swing equation is expressed as:

$$M \frac{d\omega_m}{dt} = T_m - T_e - D_p \Delta\omega_m \quad (3.13)$$

where D_p is the damping constant that represents the windage losses and friction losses of the machine, and $\Delta\omega_m = \omega_m - \omega_{m0}$.

The electromagnetic torque is defined as the derivative of the energy that is stored in the machine's magnetic field with respect to the position of the rotor [58].

$$T_e = -\frac{\partial E}{\partial \theta} \quad (3.14)$$

with i and i_f are constants. The energy is:

$$E = \frac{1}{2} \langle i, L_s i \rangle + M_f i_f \langle \mathbf{i}, \mathbf{cos} \boldsymbol{\theta} \rangle + \frac{1}{2} L_{ff} i_f^2 \quad (3.15)$$

Therefore, the torque equation is:

$$T_e = M_f i_f \langle \mathbf{i}, \mathbf{sin} \boldsymbol{\theta} \rangle \quad (3.16)$$

The relationship between the electromagnetic torque and the electromagnetic power output of a synchronous generator is:

$$T_e = \frac{P_e}{\omega_{m0}} \quad (3.17)$$

The equations described above are used in 0 to develop the frequency control loop and the VSM output voltage calculation used for reference signal generation for PWM of MMC. Besides, in CHAPTER 5, the linear model that is used to estimate the inertia is deduced based on the synchronous machine model described in this chapter. The linear model is used for the adaptive inertia estimation based on a proportional-integral, linear quadratic regulator, and model predictive controllers.

CHAPTER 4. VIRTUAL SYNCHRONOUS MACHINE

4.1 Basic Concepts

Providing virtual inertia in the system is a solution to compensate for the lack of inertia due to the RES's growing penetration level in the grid and avoid the grid's stability problems, like the increase in the rate of the change for the frequency due to disturbances in the system. The virtual inertia can be established for RES by using the conversion stage, the short term energy storage stage, and a control stage, as shown in Fig. 4.1 [2]. The virtual inertia concept was introduced in [24], called Virtual Synchronous Machine (VSM). It describes the control of the inverter that emulates the external characteristics of the conventional synchronous generator.

The idea of the VSM is based on reproducing the statics and dynamics properties of the real synchronous generator (as shown in CHAPTER 3), injecting/ absorbing active power to/from the grid [60]. The RES units will operate as a synchronous generator, exhibiting the inertia and damping properties of the grid to solve the stability problems [60]. The VSM contribute to voltage compensation during a short circuit. Hence, it can prevent the electricity grid from blackouts due to voltage instability [60]. In addition, the VSM allows controlling the frequency, voltage, active and reactive powers of the converters [60].

The VSM uses advantages of compensating the lack of inertia is [61]:

- There are no limits in the rated characteristics, as a real synchronous generator.
- The inertia and damping coefficient of the VSM can be changed upon the system response, whereas these values are fixed in a real synchronous generator.
- In the VSM, the magnetic saturation and the eddy current losses will be absent.
- It does not generate a delay in the power converter response.
- Since the VSM operates as a voltage source connected to the grid, it can supply fault currents, unbalanced and harmonic currents to non-linear loads.

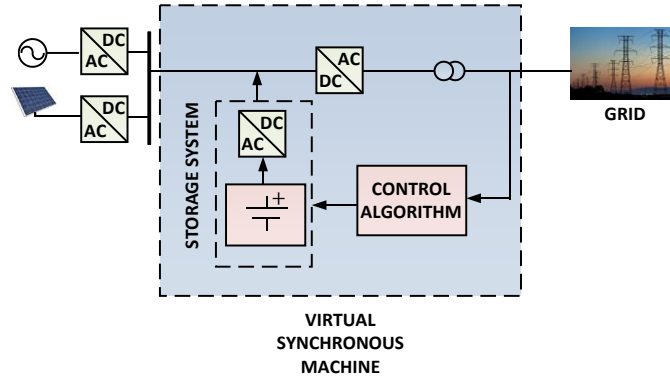


Fig. 4.1. Virtual synchronous machine.

In the specialized literature, several investigations as [10], [16], [62]-[64] have been reported, where the different synchronous machine models for implementation of the VSM are presenting, varying in their complexity. The high order models can give accurate and precise results. However, the system becomes complex when creating the algorithm that simulates its dynamics due to the computational burden. To focus in the application of the synchronous machine model, and the swing equation to emulate its external characteristics from a converter, the VSM is divided into four groups: Synchronverter, Inertia-emulation, Voltage Controlled VSM, and Current Controlled VSM [65].

The synchronverter is proposed in [58] to emulate the external characteristics of the synchronous generator using the power electronics converters. It is the simplest application of the VSM in terms of topology and complexity. This method consist in a frequency droop or real power regulation ($P - f$) (from the swing equation) and a voltage droop or voltage regulation ($Q - v$) [2].

The topology of the inertia emulation based on the use of the swing equation to calculate the power reference using the frequency, and to calculate the current reference from the power reference and the output voltage measure of the inverter, however, this method requires the Phase Locked Loop (PLL) [66].

The voltage controlled VSM topology is the most complex model, it based on the swing equation model and the frequency droop for angle and power control. It has a reactive power controller that consists of a virtual impedance and voltage reference, this method requires the cascade voltage and current controllers, but it is a complex topology due to tune the parameters of these controllers [17]. The current controlled VSM topology consists of a generalized model of the frequency droop based on the swing equation to calculate the phase

angle and VSM frequency. It has a reactive power controller using a virtual impedance and mathematical model of the synchronous machine in the cascade of the current controller. However, this topology needs more care in the virtual impedance design because it can affect the stability system [67].

In this work, the synchronverter method is used to control the MMC terminal due to simple application, and it does not require the PLL.

4.2 Frequency Drooping

The synchronous generator adjusts the output power by adjusting the prime-mover; moreover, it responds to the grid's frequency variation to maintain system stability [2], [55]. Similarly, the $P - f$ droop control is used to regulate an inverter output active power according to the grid's frequency. It allows the generation and control of the angular position and the angular speed of the VSM, which are called virtual angular and virtual angular speed (represents the angular position and angular speed of the traditional synchronous generator), respectively. The frequency droop can be implemented in the VSM by comparing the virtual angular speed with reference to angular frequency ω^* [58]. Then, the droop control is expressed as [2]:

$$\begin{aligned} M \frac{d\omega_m}{dt} &= T_m - T_e - D_p \Delta\omega_m \\ \omega_m &= \frac{d\theta}{dt} \end{aligned} \quad (4.2)$$

The parameters of $P - f$ droop control are calculated as follows:

$$D_p = -\frac{\Delta T}{\Delta\omega} \quad M = D_p \tau_f \quad T_m = \frac{P_0}{\omega_{m0}} \quad (4.3)$$

where ΔT and $\Delta\omega_m$ are the variation in the total torque and the variation in the angular frequency, respectively, τ_f is time a constant of the frequency-droop loop, and P_0 is the reference for the output active power. The $P - \omega$ droop control based on (4.2) is illustrated in Fig. 4.2.

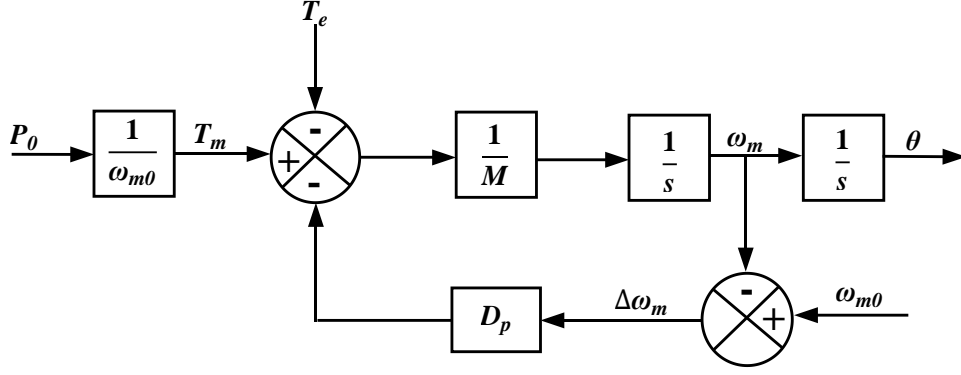


Fig. 4.2. The $P - \omega$ droop control scheme.

4.3 Voltage Drooping

The VSM reactive power and voltage control ($Q - v$ droop) are similar to the control method of a synchronous generator, which regulates the output voltage using an Automatic Regulation Voltage (AVR) [2], [55].

Therefore, the AVR system in the VSG is expressed as the difference between the amplitude of the reference voltage v_0 and the amplitude of the grid voltage v_g , multiplied by a voltage drooping constant D_q . The $Q - v$ droop control regulates the voltage by control the field excitation $M_f i_f$, which is proportional to the amplitude of the voltage generate [68], as shown in (3.8). Then, the droop control can be expressed as [2]:

$$M_f i_f = \frac{1}{K_S} \left((Q_0 - Q) + D_q (v_0 - v_g) \right) \quad (4.4)$$

where M_f is the magnitude of the mutual inductance between the field and the stator windings, i_f is the field excitation current, Q_0 is the reactive power reference, K is a reactive controller gain, D_q is the voltage droop control, Q is the VSM reactive power. The D_q and Q are calculated as:

$$Q = -\theta M_f i_f \cos \theta$$

$$D_q = -\frac{\Delta Q}{\Delta v} \quad (4.5)$$

where θ is the angle between the rotor axis and one of the stator windings phases, ΔQ is the reactive power variation, and Δv is the voltage variation.

The relationship between K and the constant time τ_v is expressed by:

$$K = D_q \tau_v \omega_{m0} \quad (4.6)$$

To obtain the grid voltage amplitude is used the amplitude detector, as shown in Fig. 4.3. Assume the grid's phase voltage as:

$$\begin{aligned} v_a &= v_g \sin \theta \\ v_b &= v_g \sin \left(\theta - \frac{2\pi}{3} \right) \\ v_c &= v_g \sin \left(\theta + \frac{2\pi}{3} \right) \end{aligned} \quad (4.7)$$

Then,

$$\begin{aligned} v_a v_b + v_b v_c + v_c v_a &= v_g^2 \sin \theta \sin \left(\theta - \frac{2\pi}{3} \right) + v_g^2 \sin \left(\theta - \frac{2\pi}{3} \right) \sin \left(\theta + \frac{2\pi}{3} \right) \\ &\quad + v_g^2 \sin \left(\theta + \frac{2\pi}{3} \right) \sin \theta \end{aligned} \quad (4.8)$$

Applying the following trigonometric identity:

$$\sin x \sin y = \frac{1}{2} (\cos(x - y) - \cos(x + y)) \quad (4.9)$$

It is possible to get:

$$\begin{aligned} v_a v_b + v_b v_c + v_c v_a &= -\frac{3}{4} v_g^2 - \frac{1}{2} v_g^2 \left(\cos \left(2\theta - \frac{2\pi}{3} \right) + \cos(2\theta) + \cos \left(2\theta + \frac{2\pi}{3} \right) \right) \end{aligned} \quad (4.10)$$

Applying the following trigonometric identity:

$$\cos x \cos y = 2 \cos \left(\frac{x + y}{2} \right) \cos \left(\frac{x - y}{2} \right) \quad (4.11)$$

It is possible to get:

$$v_g = -\frac{4}{3} \sqrt{v_a v_b + v_b v_c + v_c v_a} \quad (4.12)$$

The $Q - v$ droop control based on (4.4) is illustrated in Fig. 4.3.

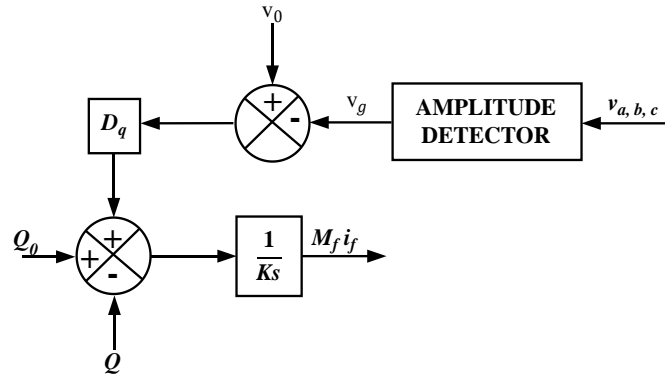


Fig. 4.3. The $Q - v$ droop control scheme.

CHAPTER 5. ADAPTIVE INERTIA FOR A VIRTUAL SYNCHRONOUS MACHINE APPLICABLE TO A MODULAR MULTILEVEL CONVERTER

5.1 Linear Model for Inertia Estimation

Based on the linear model described in (4.2), ω_m and θ are the state variables, and M and D_p are the control variables, which are estimated based on PI, LQR, and MPC controllers [2]. Hence, the model is considered a nonlinear model.

By linearizing (4.2), it is possible to get [2]:

$$\begin{aligned} \Delta \dot{\omega}_m = & -\frac{P_0}{M_0^2} \Delta M - \frac{M_f i_{f_0} \langle \mathbf{i}, \sin \theta_0 \rangle}{M_0} \Delta \omega_m - \frac{\omega_{m0} M_f i_{f_0} \langle \mathbf{i}, \cos \theta_0 \rangle}{M_0} \Delta \theta \\ & + \frac{\omega_{m0} M_f i_{f_0} \langle \mathbf{i}, \sin \theta_0 \rangle}{M_0^2} \Delta M - \frac{D_{p0}}{M_0} \Delta \omega_m - \frac{\omega_{m0}}{M_0} \Delta D_p + \frac{D_{p0} \omega_{m0}}{M_0^2} \Delta M \\ \Delta \dot{\theta} = & \Delta \omega_m \end{aligned} \quad (5.2)$$

where $M_0, M_f i_{f_0}, \omega_{m0}, \theta_0, D_{p0}$ are the initial conditions of the linear system.

Considering (5.2), the state-space model is represented as [2]:

$$\begin{aligned} A = & \begin{bmatrix} \left(-\frac{M_f i_{f_0} \langle \mathbf{i}, \sin \theta_0 \rangle}{M_0} - \frac{D_{p0}}{M_0} \right) & -\frac{\omega_{m0} M_f i_{f_0} \langle \mathbf{i}, \cos \theta_0 \rangle}{M_0} \\ 1 & 0 \end{bmatrix} \\ B = & \begin{bmatrix} \left(-\frac{P_0}{M_0^2} + \frac{\omega_{m0} M_f i_{f_0} \langle \mathbf{i}, \sin \theta_0 \rangle}{M_0^2} + \frac{D_{p0} \omega_{m0}}{M_0^2} \right) & -\frac{\omega_{m0}}{M_0} \\ 0 & 0 \end{bmatrix} \\ C = & \begin{bmatrix} 1 & 0 \\ 0 & 1 \end{bmatrix} \quad D = \begin{bmatrix} 0 & 0 \\ 0 & 0 \end{bmatrix} \end{aligned} \quad (5.3)$$

The input and state vectors are defined as:

$$\begin{aligned} u &= [\Delta M \quad \Delta D_p]^T \\ x &= [\Delta \omega_m \quad \Delta \theta]^T \end{aligned} \quad (5.4)$$

The inertia and damping factor are estimated using PI, LQR, and MPC controllers, considering the state-space model in (5.3), as shown in sections 5.2, 5.3, and 5.4.

5.2 Adaptive Inertia using a PI Controller

In the VSM concept, large virtual inertia requires large energy storage systems (e.g., inductors and capacitors) in the converter. On the other hand, reduced virtual inertia has less energy storage requirements but operates faster; however, this may not be adequate to recover the frequency within thresholds after a disturbance [69]. In this sub-section a Virtual Synchronous Machine with an adaptive inertia (VSM-PI) is proposed. The adaptive inertia ΔM is calculated as follows:

$$\begin{aligned}\Delta M &= k_p e + k_i e \\ e &= \omega_{m0} * T_e - \omega_m * T_m\end{aligned}\tag{5.6}$$

where k_p and k_i are proportional and integral constants, respectively, e is the error calculated as the cross error of the active power and the VSM frequency. This control aims to minimize the power oscillations and frequency droop in the system with a fast response.

The virtual inertia is calculated as follows:

$$M = \begin{cases} M_0, & |\Delta\omega| \leq K \\ M_0 + |\Delta M|, & |\Delta\omega| > K \end{cases}\tag{5.7}$$

where K is the deviation frequency threshold, which equals to 0.0005 pu according to the dead-band for the Colombian power system. The VSM-PI controller based on (5.6) is illustrated in Fig. 5.1.

5.3 Adaptive Inertia using Linear Quadratic Regulator (LQR) Controller

The VSM-LQR controller objective is to calculate the inertia and damping constants, guaranteeing the optimal balance between the fast frequency response and the frequency oscillations in the power system disturbances presence [2].

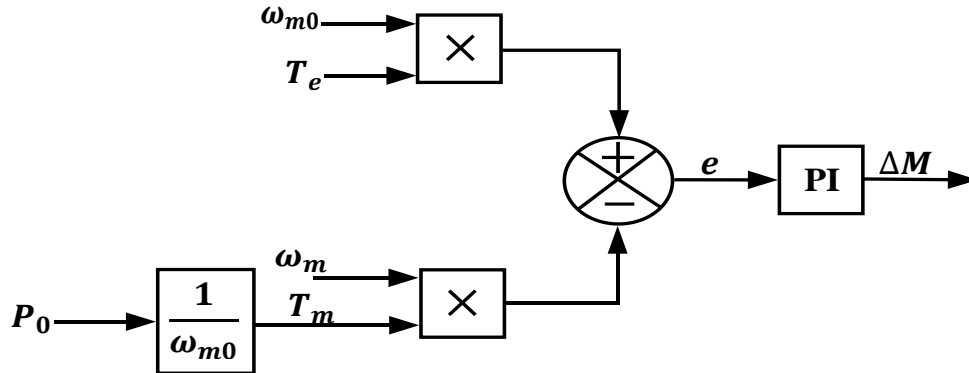


Fig. 5.1. The VSM-PI controller scheme.

Considering that $\Delta M = M - M_0$, and $\Delta D_p = D_p - D_{p_0}$, the virtual inertia and damping coefficient are calculated as follows [69]:

$$\begin{bmatrix} M \\ D_p \end{bmatrix} = \begin{bmatrix} M_0 \\ D_{p_0} \end{bmatrix} + \begin{bmatrix} \Delta M \\ \Delta D_p \end{bmatrix} \quad (5.7)$$

where ΔD_p is the adaptive damping coefficient, which is computed using the LQR control theory as follows [2]:

$$\begin{bmatrix} \Delta M \\ \Delta D_p \end{bmatrix} = - \begin{bmatrix} L_M & L_D \\ L_D & L_D \end{bmatrix} \begin{bmatrix} \Delta \omega \\ \Delta \theta \end{bmatrix} \quad (5.8)$$

where \mathbb{L} is the feedback matrix gain.

The state-space model that is used for the controller is presented in (5.3), and the quadratic cost function is [69] as shown following:

$$\begin{aligned} \min \int_0^\infty \frac{1}{2} (x^T Q x + u^T R u) dt \\ \text{s.t. } \begin{cases} \dot{x} = Ax + B\Delta u \\ \Delta u = -Lx \end{cases} \end{aligned} \quad (5.9)$$

where x is the state variables, u is the input variables, as shown in (5.4), Q is the error penalty factor, and R is the control signal penalty factor. Optimizing (5.9) yields into the optimal feedback control gains, as follows [2]:

$$K_i^* = R^{-1} B^T P \quad (5.10)$$

where P is the solution to the algebraic Riccati equation [69]:

$$A^T P + P A - P B R^{-1} B^T P + Q = 0 \quad (5.11)$$

The VSM controller parameters are realized through a state feedback control scheme, as shown in Fig. 5.2.

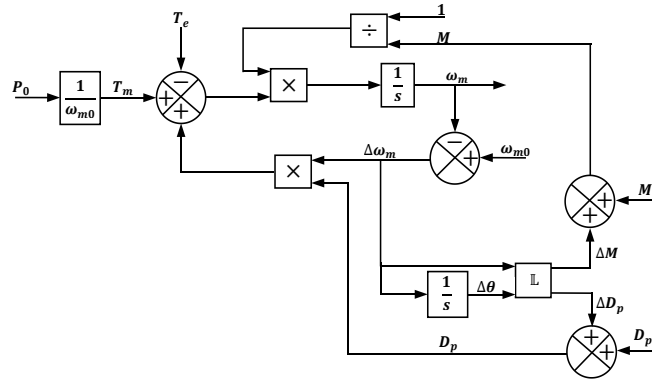


Fig. 5.2. The VSM-LQR controller schematic.

5.4 Adaptive Inertia using Model Predictive Control (MPC) Controller

The MPC is an optimal control technique widely used in industrial process applications. The main objective of MPC is to determine an optimal trajectory of outputs y with minimal cost of the input signals u . This control technique has some advantages over other techniques such as the management of multiple variables, the introduction of restrictions in the design process, and the intrinsic compensation in the dead times [70]. However, the algorithm's complexity increases the computational burden as well as the need to implement an optimization algorithm.

A discrete linear dynamic system is described as:

$$\begin{aligned} x_m(k+1) &= A_m x_m(k) + B_m u(k) \\ y(k) &= C_m x_m(k), \end{aligned} \quad (5.12)$$

where $x_m(k)$, $u(k)$, and $y(k)$ are the state, inputs, and outputs vectors of the system at the sample k , respectively. Matrices A_m , B_m , and C_m are the state-space matrices. Defining the incremental variables as:

$$\begin{aligned} \Delta x_m(k+1) &= x_m(k+1) - x_m(k) \\ u(k+1) &= u(k) - u(k-1). \end{aligned} \quad (5.13)$$

By replacing (5.13) in (5.12) is possible to get:

$$\begin{aligned} \Delta x_m(k+1) &= A_m(x_m(k) - x_m(k-1)) + B_m(u(k) - u(k-1)) \\ &= A_m \Delta x_m(k) + B_m \Delta u(k) \end{aligned} \quad (5.14)$$

To link $\Delta x_m(k)$ to the output $y(k)$, a new state vector is created as:

$$x(k) = \begin{bmatrix} \Delta x_m(k)^T \\ y(k) \end{bmatrix} \quad (5.15)$$

Therefore, the output of the system is described as:

$$\begin{aligned} y(k+1) - y(k) &= C_m(x_m(k+1) - x_m(k)) \\ &= C_m \Delta x_m(k+1) = C_m A_m \Delta x_m(k) + C_m B_m \Delta u(k) \end{aligned} \quad (5.16)$$

Substituting (5.14) in (5.13) the following state-space model is obtained:

$$\begin{aligned} x(k+1) &= A_a x(k) + B_a \Delta u(k) \\ y(k) &= C_a \begin{bmatrix} \Delta x_m(k) \\ y(k) \end{bmatrix}, \end{aligned} \quad (5.17)$$

with,

$$A_a = \begin{bmatrix} A_m & 0 \\ C_m A_m & 1 \end{bmatrix} \quad B_a = \begin{bmatrix} B_m \\ C_m B_m \end{bmatrix} \quad C_a = [0 \quad 1] \quad (5.18)$$

The state predictions are:

$$\begin{aligned} x(k_i + 1|k_i) &= A_a x(k_i) + B_a \Delta u(k_i) \\ x(k_i + 2|k_i) &= A_a x(k_i + 1|k_i) + B_a \Delta u(k_i + 1) \\ x(k_i + N_p|k_i) &= A_a^{N_p} x(k_i) + A_a^{N_p-1} B_a \Delta u(k_i) + A_a^{N_p-2} B_a \Delta u(k_i + 1) + \dots \\ &\quad + A_a^{N_p-N_c} B_a \Delta u(k_i + N_c - 1) \end{aligned} \quad (5.19)$$

The state prediction is increased to reach a prediction horizon N_p , with control horizon N_c , where $N_c < N_p$. In the prediction of the output:

$$\begin{aligned} y(k_i + 1|k_i) &= C A_a x(k_i) + C_a B_a \Delta u(k_i) \\ y(k_i + 2|k_i) &= C A_a^2 x(k_i) + C A_a B_a \Delta u(k_i) + C B_a \Delta u(k_i + 1) \\ y(k_i + N_p|k_i) &= C_a A_a^{N_p} x(k_i) + C_a A_a^{N_p-1} B_a \Delta u(k_i) \\ &\quad + C_a A_a^{N_p-2} B_a \Delta u(k_i + 1) + \dots + A_a^{N_p-N_c} B_a \Delta u(k_i + N_c - 1) \end{aligned} \quad (5.20)$$

All predictions are formulated in terms of actual state variables $x(k_i)$ and future control signals $\Delta u(k_i + j)$, where $j = 0, 1, \dots, N_c - 1$. Therefore, the vectors are defined as:

$$\begin{aligned} Y &= [y(k_i + 1|k_i) \quad y(k_i + 2|k_i) \quad \dots \quad y(k_i + N_p|k_i)]^T \\ \Delta U &= [\Delta u(k_i) \quad \Delta u(k_i + 1) \quad \dots \quad \Delta u(k_i + N_c - 1)]^T, \end{aligned} \quad (5.21)$$

where Y is the output vector prediction, and ΔU is the vector of future control signals. The predictions of the output are calculated as:

$$\begin{aligned} Y &= Fx(k_i) + G\Delta U \\ F &= \begin{bmatrix} C_a A_a \\ C_a A_a^2 \\ C_a A_a^3 \\ \vdots \\ C_a A_a^{N_p} \end{bmatrix} \\ G &= \begin{bmatrix} C_a B_a & 0 & 0 & \dots & 0 \\ C_a A_a B_a & C_a B_a & 0 & \dots & 0 \\ C_a A_a^2 B_a & C_a A_a B_a & C_a B_a & \dots & 0 \\ \vdots & \vdots & \vdots & \ddots & \vdots \\ C_a A_a^{N_p-1} B_a & C_a A_a^{N_p-2} B_a & C_a A_a^{N_p-3} B_a & \dots & C_a A_a^{N_p-N_c} B_a \end{bmatrix} \end{aligned} \quad (5.22)$$

The vector with the optimal parameters ΔU , at the time k_i , is found using:

$$\Delta U = (G^T G + \bar{R})^{-1} (G^T R_s - G^T F x(k_i)) \quad (5.23)$$

where $(G^T G + \bar{R})^{-1} G^T R_s$ is the set-point change, $(G^T G + \bar{R})^{-1} G^T F x(k_i)$ is the state feedback control of predictive control, $\bar{R} = rI$. I is the identity matrix and $r \geq 0$ is a control gain that affects the control [71]. R_s is the reference vector. The set-point change and the state feedback control depend on the system parameters and the constant matrices are invariant over time. The first element of ΔU at time k_i is:

$$\begin{aligned} \Delta u(k_i) &= [1 \quad 0 \cdots 0 \quad N_c] (G^T G + \bar{R})^{-1} (G^T \bar{R}_s r(k_i) - G^T F x(k_i)) \\ &= k_y r(k_i) - k_{mpc} x(k_i) \end{aligned} \quad (5.24)$$

where N_c is the horizon control, k_y is the first element of $(G^T G + \bar{R})^{-1} G^T \bar{R}_s$, k_{mpc} is the first row of $(G^T G + \bar{R})^{-1} G^T F$.

Applying the MPC to the model presented in (5.3), the augmented matrices A_a, B_a, C_a are:

$$\begin{aligned} A_a &= \begin{bmatrix} \left(-\frac{M_f i_{f_0} \langle i, \sin \theta_0 \rangle}{M_0} - \frac{D_{p_0}}{M_0} \right) & -\frac{\omega_{m_0} M_f i_{f_0} \langle i, \cos \theta_0 \rangle}{M_0} & 0 & 0 \\ 1 & 0 & 0 & 0 \\ \left(-\frac{M_f i_{f_0} \langle i, \sin \theta_0 \rangle}{M_0} - \frac{D_{p_0}}{M_0} \right) & -\frac{\omega_{m_0} M_f i_{f_0} \langle i, \cos \theta_0 \rangle}{M_0} & 1 & 0 \\ 1 & 0 & 0 & 1 \end{bmatrix} \\ B_a &= \begin{bmatrix} \left(-\frac{P_0}{M_0^2} + \frac{\omega_{m_0} M_f i_{f_0} \langle i, \sin \theta_0 \rangle}{M_0^2} + \frac{D_{p_0} \omega_{m_0}}{M_0^2} \right) & -\frac{\omega_{m_0}}{M_0} \\ 0 & 0 \\ \left(-\frac{P_0}{M_0^2} + \frac{\omega_{m_0} M_f i_{f_0} \langle i, \sin \theta_0 \rangle}{M_0^2} + \frac{D_{p_0} \omega_{m_0}}{M_0^2} \right) & -\frac{\omega_{m_0}}{M_0} \\ 0 & 0 \end{bmatrix} \\ C_a &= \begin{bmatrix} 0 & 0 & 1 & 0 \\ 0 & 0 & 0 & 1 \end{bmatrix} \end{aligned} \quad (5.25)$$

Based on the augmented matrices (5.25) and the vector with the optimal parameters ΔU (5.23) is predicted the control signals ΔM and ΔD_p to calculate the inertia and damping coefficient according to (5.7).

CHAPTER 6. SIMULATIONS AND RESULTS

The adaptive inertia control scheme proposed in CHAPTER 5 has been validated through simulations on the MMC terminal illustrated in Fig. 2.1, which parameters are listed in Table 6.1. The MMC control scheme is presented in Fig. 6.1, whereas the initial conditions of the linear model to estimate the inertia are listed in Table 6.2. Extensive time-domain simulations to evaluate the performance of the VSM (constant inertia), VSM-PI, VSM-LQR, and the VSM-MPC control schemes (CHAPTER 5), are carry out in Matlab/Simulink with a simulation time of 1500 ms. For the experiment, changes in the active and reactive powers are made to evaluate the controllers' performance. The variables to be controlled are the output active and reactive powers, and the VSM frequency.

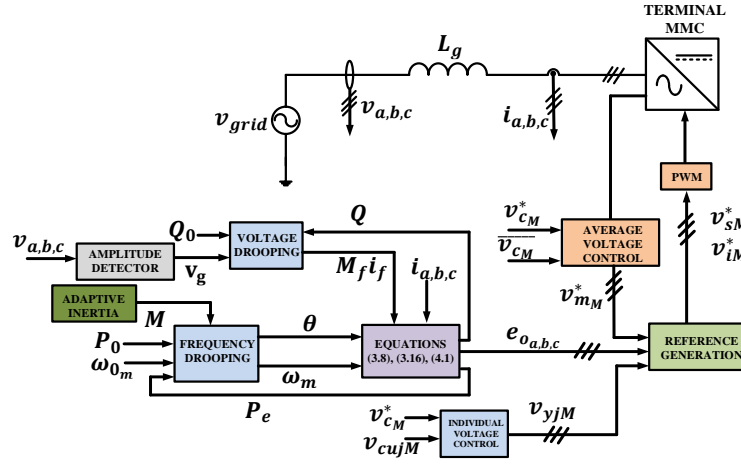


Fig. 6.1. MMC controller schematic.

TABLE 6.1. SYSTEM PARAMETERS

Parameter	Symbol	Value
dc Voltage	V_{dc}	200 kV
ac Voltage	V_{ac}	115 kV
Arm Inductance	L_a	7 mH
Arm Resistance	R_a	0.1 Ω
No. of Arm's Submodules	N	7
Submodule Capacitance	C	2000 μ F
Grid Inductance	L_g	28 mH
Grid Resistance	R_g	0.79 Ω
Base Power	S_{base}	200 MVA
Base Inductance	L_{base}	0.18 H
Base Impedance	Z_{base}	66.13 Ω
Switching Frequency	f_{sw}	2 kHz
Fundamental Frequency	f_1	60 Hz

TABLE 6.2. LINEAR SYSTEM: INITIAL CONDITIONS

Parameter	Symbol	Value (pu)
Initial Inertia Constant	M_0	0.1
Initial Damping Coefficient	D_{p_0}	100
Initial Field Excitation Z	$M_f i_{f_0}$	1
Initial Angular Speed	ω_{m0}	1
Initial Angle	θ_0	0

6.1 The MMC output active power

The measured active power at the MMC output, and the one calculated by the VSM with constant inertia controller, are illustrated in Fig. 6.2. Notice that the VSM approach has a good performance to control the active power without overshoot, the settling time is 180 ms, and the steady-state error is 5.914 %. In addition, in steady-state, the active power oscillates

around the reference with 24 MW amplitude for the VSM (constant inertia). After 500 ms, the power oscillations increase to 45 MW due to the reactive power reference variation.

The active power at the MMC output calculated by the VSM-PI, the VSM-LQR, and using the VSM-MPC controller is illustrated in Fig. 6.3. Notice that the three controllers control the active power without overshoot, and the settling time is decreased to 160 ms with VSM-PI; 130 ms with the VSM-LQR and VSM-MPC compare to VSM (constant inertia). The steady-state error is reduced to 4.927 %, 4.668 %, and 3.660 %, respectively, compare to VSM (constant inertia). Besides, in steady-state, the active power oscillations around the reference is reduced to 19 MW with VSM-PI, 10 MW with VSM-LQR, and VSM-MPC, compare to VSM. After 500 ms, the power oscillations increase to 33 MW for VSM-PI, VSM-LQR, and 30 MW for VSM-MPC due to the reactive power reference variation.

The active power oscillations increase due to reactive power reference variation because the active power loop and reactive power loop has a dependency between them because the reactive power loop estimates the $M_f i_f$ parameter necessary for calculating the VSM electrical torque and the VSM active power that are part of the active power control.

Notice that the VSM-MPC approach has a better performance by reducing the oscillations in steady-state and the steady-state error. Moreover, the VSM-LQR and VSM-MPC present less settling time than VSM with constant inertia and the VSM-PI.

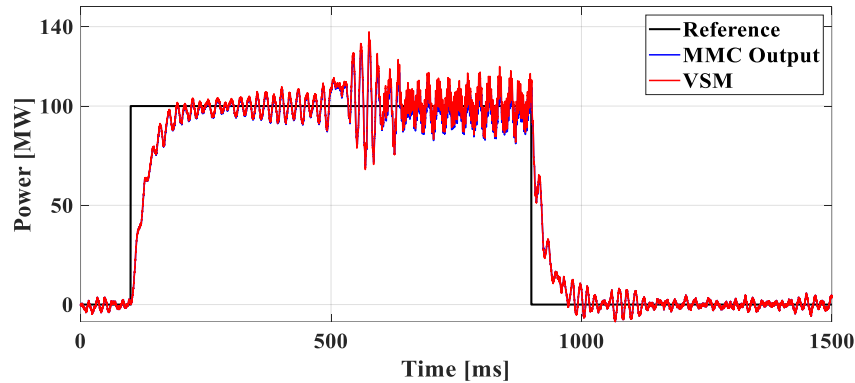
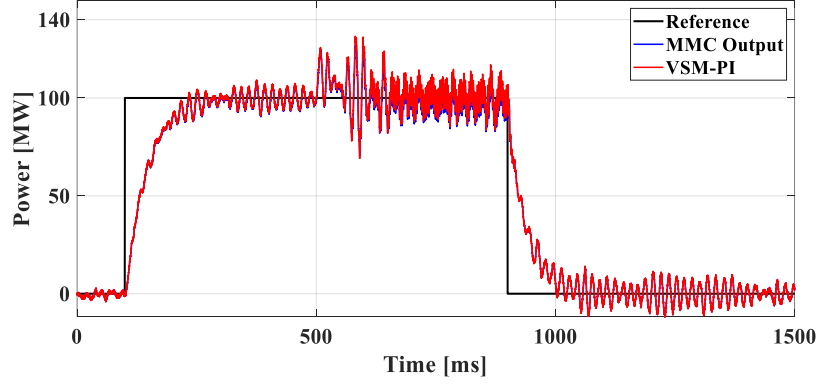
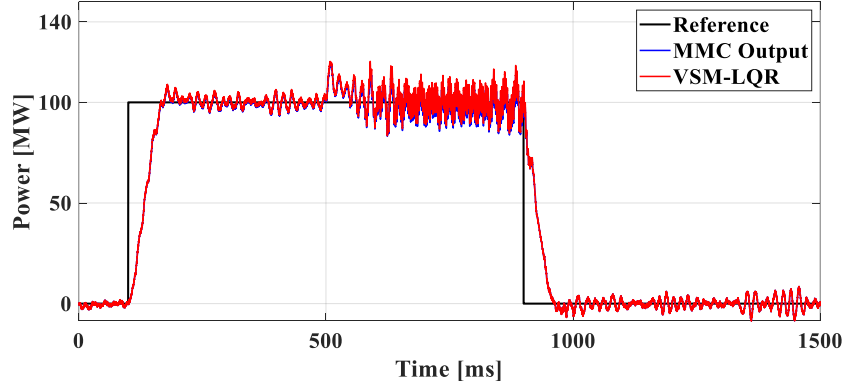


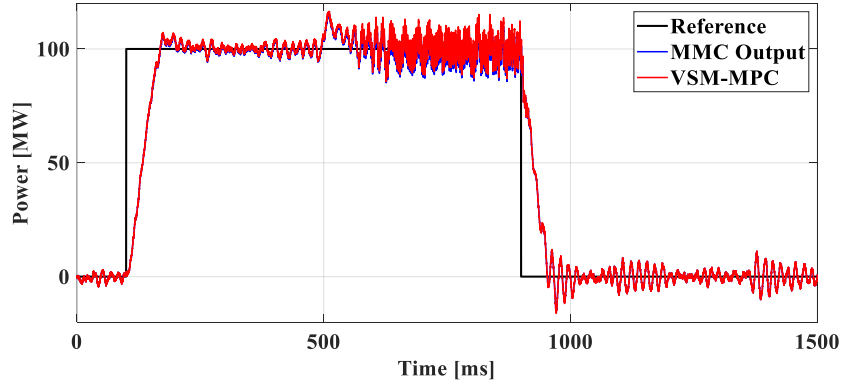
Fig. 6.2. Comparison of the output active power of the MMC with the power estimated by the VSM controller.



(a)



(b)



(c)

Fig. 6.3. Comparison of the output active power of the MMC with the power estimated by the VSM-PI (a), VSM-LQR (b) and VSM-MPC (c) controllers.

6.2 The MMC output reactive power

The reactive power at the MMC output calculated using the VSM with constant inertia controller is illustrated in Fig. 6.4. As shown, the reactive power does not present the

overshoot. The settling time is 250 ms, and the steady-state error is 0.115 %. In steady-state, the reactive power oscillates around the reference with an amplitude of 25 MW.

Notice in the figure that the reactive power at the output of the MMC is smaller than the reactive power estimated by the VSM controller because of the action of the filter.

The reactive power at the output of the MMC calculated with the VSM-PI, the VSM-LQR, and the VSM-MPC controller, are illustrated in Fig. 6.5. As shown, the reactive power signal does not present overshoot, as in the case of VSM with constant inertia. The settling time is 250 ms with the three controllers. The steady-state error is reduced to 4.927 % for VSM-PI, 3.519 % for VSM-LQR, and 3.660 % for VSM-MPC.

In steady-state, the reactive power oscillates around the reference with an amplitude of 25 MW for VSM-PI and VSM-LQR controllers, and 23 MVar for VSM-MPC controller.

Note in the Fig. 6.5 that the reactive power at the output of the MMC is smaller than the reactive power estimated by the VSM controller because of the action of the filter. Moreover, VSM-PI, VSM-LQR, and VSM-MPC present less settling time and steady-state error than VSM with constant inertia. The VSM-MPC presents less reactive power oscillates than VSM with constant inertia, VSM-PI, and VSM-LQR.

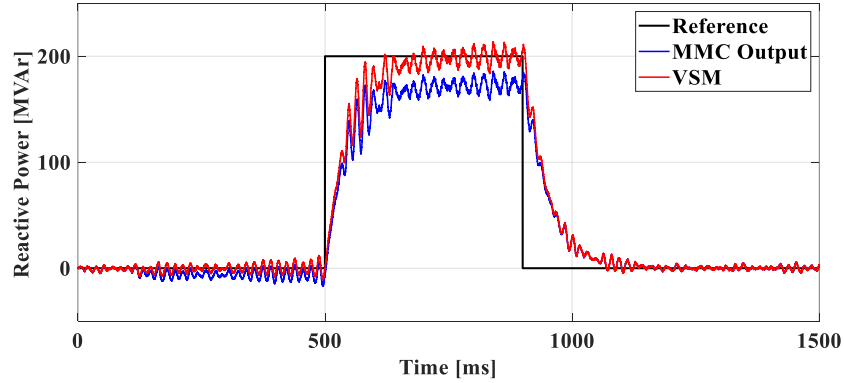
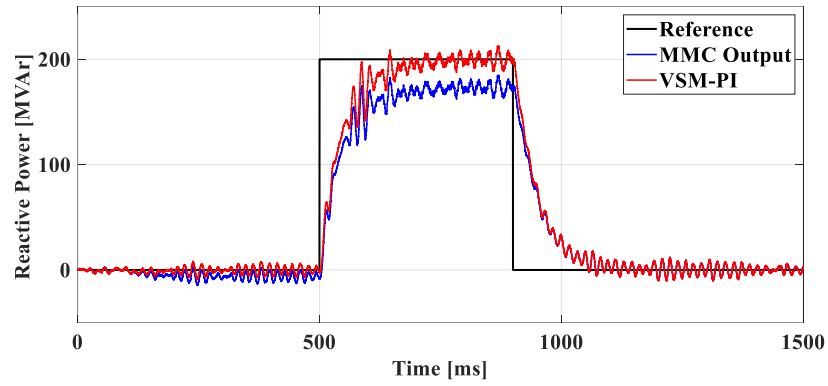
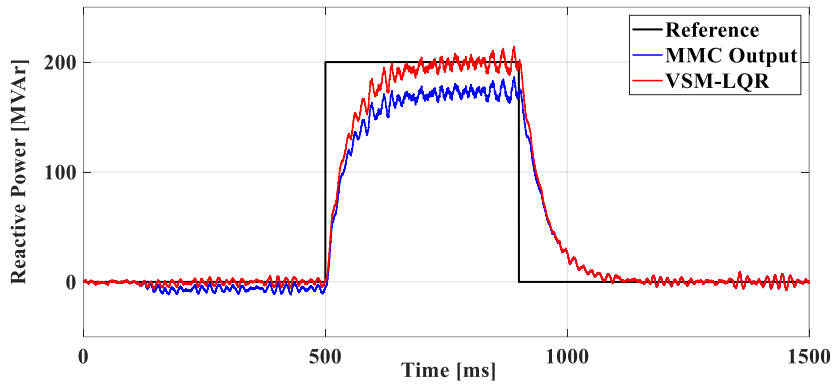


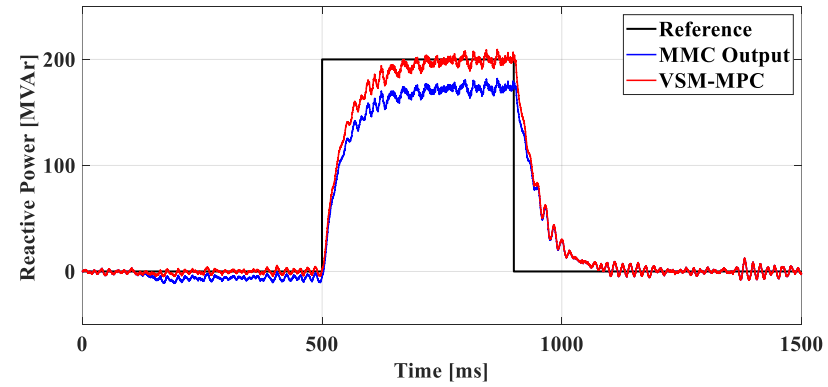
Fig. 6.4. Comparison of the output reactive power of the MMC with the power estimated by the VSM controller.



(a)



(b)



(c)

Fig. 6.5. Comparison of the output reactive power of the MMC with the power estimated by the VSM-PI (a), VSM-LQR (b) and VSM-MPC (c) controllers.

6.3 VSM dynamic frequency response

Fig. 6.6 illustrates the VSM frequency signal with constant inertia. The variations in the power reference generate frequency disturbances with a maximum value of 60.267 Hz and a minimum value of 59.754 Hz with a settling time of 150 ms. In steady-state, the frequency oscillates around the reference with an amplitude of 0.042 Hz. After 500 ms, the oscillations increase to 0.072 Hz due to reactive power reference variation.

Finally, the rate change of the frequency (ROCOF) with VSM (constant inertia) is 3.424 Hz/s.

Fig. 6.7 illustrates the VSM frequency signal with the estimated inertia using PI, LQR, and MPC controllers (described in CHAPTER 5). The frequency disturbances due to changes in the power references are reduced with three controllers. The maximum frequency is decreased to 60.180 Hz for VSM-PI; 60.177 Hz for VSM-LQR and VSM-MPC. The minimum frequency is reduced to 59.833 Hz, 59.842 Hz, and 59.844 Hz, respectively. In steady-state, the frequency oscillation is 0.035 Hz, 0.024 Hz, and 0.022 Hz for the VSM-PI, VSM-LQR, and VSM-MPC, respectively, and the settling time is 150 ms for VSM-PI and 80 ms for VSM-LQR and VSM-MPC. The oscillations increase to 0.060 Hz, 0.046 Hz, and 0.023 Hz after 500 ms, due to reactive power variation.

Notice that the VSM-LQR and VSM-MPC have presented similar maximum values and the settling time. But, the VSM-MPC approach has a better performance by reducing the minimum frequency value.

On the other hand, the VSM frequency with VSM-PI, VSMP-LQR, and VSM-MPC has a ROCOF of 2.096 Hz/s, 3.672 Hz/s, and 2.692 Hz/s, respectively.

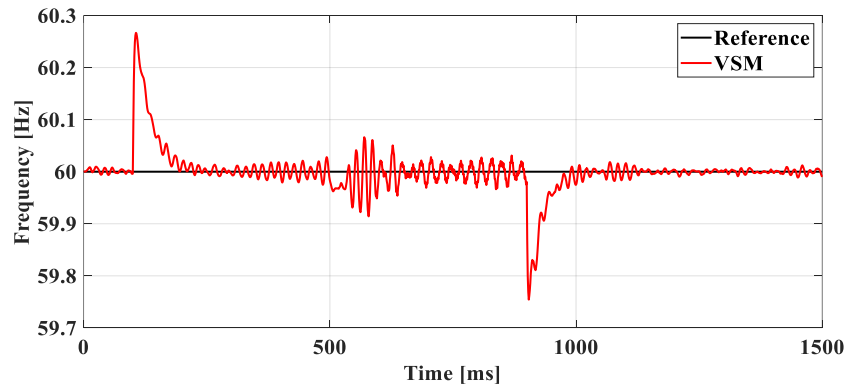
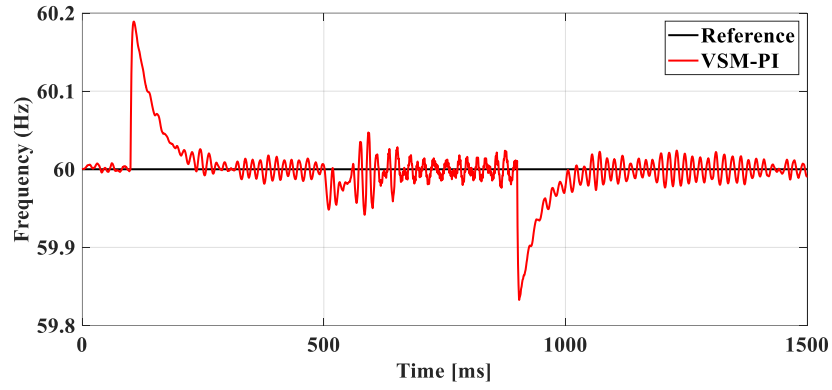
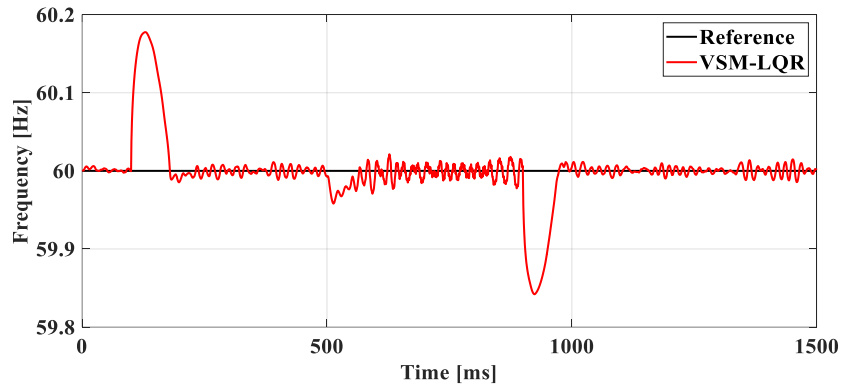


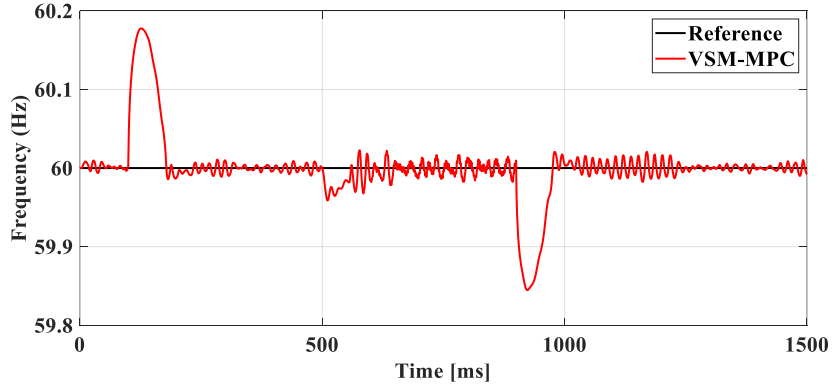
Fig. 6.6. The frequency of the VSM with constant inertia.



(a)



(b)



(c)

Fig. 6.7. The VSM frequency with the estimated inertia using PI (a), LQR (b), and MPC (c) controllers.

6.4 Analysis of the results

The summary of the results is listed in Table 6.3. Notice that the VSM-MPC approach has a better performance than other controllers; this is it reduces the steady-state error of

frequency, active power, and reactive power, reducing the frequency ROCOF. The VSM-MPC values of settling time, minimum, and maximum frequency are similar to the VSM-LQR. Nevertheless, the settling time is 70 ms less than VSM-PI.

The VSM-MPC has less ROCOF than VSM-LQR. However, it has greater ROCOF than VSM-PI, which indicates that by decreasing the settling time and steady-state error significantly, the rate change of frequency increases, despite the minimum and maximum frequency reduction compared to VSM-PI.

In Fig. 6.8, the frequency errors are presented. This error is calculated by subtracting from the estimated frequency by VSM, the desired reference. Notice that the VSM-LQR and VSM-MPC have less error in Hz than other controllers. In $t=500$ ms, the disturbance due to reactive power variation is presented, but the frequency error for all controllers is less than 1 % of the base frequency (60 Hz).

TABLE 6.3. THE RESULTS SUMMARY.

Variable	Parameter	VSM	VSM-PI	VSM-LQR	VSM-MPC
Frequency	Minimum	59.754 Hz	59.833 Hz	59.842 Hz	59.844 Hz
	Maximum	60.267 Hz	60.189 Hz	60.177 Hz	60.177 Hz
	Settling Time	150 ms	150 ms	80 ms	80 ms
	ROCOF	3.424 Hz/s	2.096 Hz/s	3.672 Hz/s	2.692 Hz/s
	Steady-State Error	0.030 %	0.020 %	0.014 %	0.007%
Active Power	Settling Time	180 ms	160 ms	130 ms	130 ms
	Steady-State Error	5.914 %	4.927 %	4.668 %	3.660 %
Reactive Power	Settling Time	250 ms	250 ms	250 ms	250 ms
	Steady-Time Error	9.115 %	8.621 %	8.278 %	8.268 %

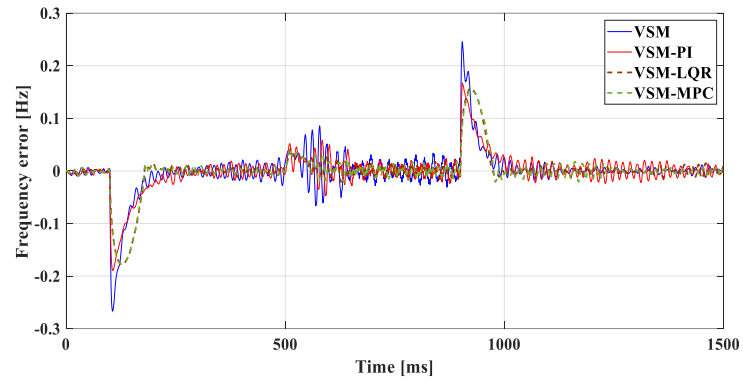


Fig. 6.8. The frequency error.

CHAPTER 7. CONCLUSIONS

This research work presented the simulation and evaluation of the VSM with constant inertia and adaptive inertia applied to a HVDC-MMC inverter emulating a VSM. The active and reactive powers of the MMC and the VSM frequency were the control variables. To compare the operation during active and reactive power changes, four techniques were used: VSM with the constant inertia, VSM-PI, VSM-LQR, and VSM-MPC.

The steady-state error, settling time, and overshoot of the control variables were considered to evaluate the controllers' performance. The LQR and MPC control schemes presented a better performance to reduce the frequency overshoots for active power variations, as shown in section 6.1. The minimum and maximum overshoot frequency with LQR and MPC control techniques to estimate inertia was 60.177 Hz and 59.82 Hz, respectively. The minimum and maximum values with constant inertia and PI control were 60.267 Hz-59.754 Hz, and 60.189 Hz-59.833. Thus, the LQR and MPC reduced the overshoots frequency by 0.15 % compared to constant inertia, and by 0.02 % compared with a PI controller. In addition, the LQR and MPC control presented a similar reduction in the settling time of 70 ms in the frequency signal compared to PI and constant inertia. However, it is observed that PI shows a decrease of ROCOF in 1.328 Hz/s, 1.576 Hz/s, and 0.596 Hz/s compared with other control techniques for VSM inertia estimate. Nevertheless, the value of frequency oscillations with MPC is attenuated by 60.44 %, 37.14, and % 8.33 % in contrast with VSM, VSM-PI, VSM-LQR, respectively. Allowing conclude that the VSM-MPC presents better behavior when estimating inertia, as shown in the decrease of frequency oscillations, as presented in CHAPTER 6.

In terms of power, the VSM-LQR and VSM-MPC have decreased the active power settling time by 50 ms compared with the constant inertia controller, and 30 ms compared with VSM-PI. The VSM-MPC controller presented less steady-state error with a value of 3.66 %, reducing by 38.11 %, 13.54 %, and 25.60 % compared to the VSM, VSM-PI, and VSM-LQR. In conclusion, the MPC used to estimate the inertia had a high impact on reducing the steady-state error of the active power, which indicates that the frequency variation had effects on the active power loop. Finally, the controllers had the same performance in the reactive power settling time. However, the VSM-MPC reduced the steady-state error to 9.29 %, 4.1 %, and 0.12 % compared to other controllers. Therefore, the

inertia estimation with the MPC has an impact on reducing the steady-state error in the reactive power. Nevertheless, this reduction was not significant, as shown in the active power results.

Finally, the MPC controller to estimate the inertia of VSM was presented less steady-state error, oscillations, and settling time in frequency and active power signals. However, in terms of the reactive power signal, the performance is the same concerning settling time. The steady-state error is reduced when the MPC controller is used.

REFERENCES

- [1] O.O. Mohammed, A.O. Otuoze, S. Salisu, O. Ibrahim, N.A. Rufa'I, "Virtual synchronous generator: an overview," in *Nigerian Journal of Technology*, 2019, vol. 38, no 1, pp. 153–164.
- [2] A. J. Marin-Hurtado, W. J. Gil-Gonzalez, A. Escobar Mejia, "Adaptive Inertia for a Virtual Synchronous Machine Using a LQR Controller Applicable to a High-Voltage DC Terminal," in *Proceedings of the 2020 IEEE Technology and Innovation for Andean Industry (ANDESCON)*, to be published.
- [3] D. Shrestha, U. Tamrakar, N. Malla, Z. Ni, R. Tonkoski, "Reduction of Energy Consumption of Virtual Synchronous Machine Using Supplementary Adaptive Dynamic Programming," in *Proceedings of 2016 IEEE International Conference on Electro Information Technology (EIT)*, United State, 2016.
- [4] B. Hammer, C. Fuhr, J. Hanson, U. Konigorski, "Effects of Virtual Inertia on Stability and Power Sharing in Inverter-Based Power Systems," in *Proceedings of 2019 International Conference on Clean Electrical Power (ICCEP)*, Otranto, Italy, 2019.
- [5] C. Robles-Algarin, O. Rodríguez-Álvarez. "Un panorama de las energías renovables en el Mundo, Latinoamérica y Colombia," in *Espacios Journal*, 2018, vol. 39, no 34, pp. 10–24.
- [6] Grupo de Generación, "Informe Mensual de Variables de Generación y del Mercado Eléctrico Colombiano" [online]. UPME, Colombia, febrero, 2017, Available on: http://www.siel.gov.co/portals/0/generacion/2017/Informe_de_variables_Feb_2017.pdf.
- [7] Y. Ma, W. Cao, L. Yang, F. Wang, L.M. Tolbert, "Virtual Synchronous Generator Control of Full Converter Wind Turbines with Short-Term Energy Storage," in *IEEE Transactions On Industrial Electronics*, vol. 64, November, 2017, pp. 8821–8830.
- [8] J. Cao, W. Du, H. Wang, M. McCulloch, "Optimal Sizing and Control Strategies for Hybrid Storage System as Limited by Grid Frequency Deviations," in *IEEE Transactions on Power Systems*, vol. 14, August, 2015, pp. 1–9.
- [9] W. J. Gil-González, "Passivity-Based Control and Stability Analysis for Hydro-Solar Power System," Doctoral Thesis, doctorate in engineering, Universidad Tecnológica de Pereira, Pereira, 2019.
- [10] H. Bevrani, T. Ise, Y. Miura, "Virtual Synchronous Generators: A Survey and New Perspectives," in *Proceedings of International Journal of Electrical Power and Energy Systems (IJPES)*, 2014, vol. 54, pp. 244–254.
- [11] G. Delille, B. Francois, G. Malarange, "Dynamic Frequency Control Support by Energy Storage to Reduce the Impact of Wind and Solar Generation on Isolated Power System's inertia," in *IEEE Transaction Sustainable Energy*, vol. 3, October, 2012, pp. 931–939.

- [12] J. Si, Y. Wang, "Online Learning Control by Association and Reinforcement," in *Proceedings of the International Joint Conference on IEEE-INNS-ENNS*, vol. 3, 2000, pp. 221–226.
- [13] T. Kerdphol, M. Watanabe, K. Hongesombut, Y. Mitani, "Self-adaptive virtual inertia control-based fuzzy logic to improve frequency stability of microgrid with high renewable penetration," in *IEEE Access*, vol. 7, pp. 76 071–76 083, 2019.
- [14] T. Li, H. Cui, R. Pan, L. Wang, "VSG Virtual Inertial Control Strategy Based on Lead-lag and Fuzzy Logic Control," in *Proceedings of 2019 Chinese Automation Congress (CAC)*, China, 2019.
- [15] Y. Chen, R. Hesse, D. Turschner, "Investigation of the virtual synchronous machine in the islanded mode," in *Proceeding of Innovative Smart Grid Technologies (ISGT Europe)*, Berlin, Germany, October, 2012, pp: 14–17.
- [16] Y. Hiraase, K. Abe, K. Sugimoto, Y. Shindo, "A grid-connected inverter with virtual synchronous generator model of algebraic type," in *IEEJ on Power and Energy*, vol.184, no. 4, pp. 10–21, 2013.
- [17] S. D'Arco, J. A. Suul, O. B. Fosfo, "A virtual synchronous machine implementation for distributed control of power converter in SmartGrids," in *Electronic Power System Research*, vol.122, no. 1, 2015, pp. 180–197.
- [18] E. Rakhshani, D. Remon, A. M. Cantarellas, P. Rodriguez, "Analysis of derivative control based virtual inertia in multi-area high-voltage direct current interconnected power system," in *IET Generation, Transmission, and Distribution Journal*, vol. 10, no. 6, April, 2016, pp. 1458–1469.
- [19] E. Rakhshani, D. Remon, A. M. Cantarellas, J. M. Garcia, P. Rodriguez, "Virtual synchronous power strategy for multiple HVDC interconnections of multi-area AGC power system," in *IEEE Transaction on Power System*, vol. 32, no. 3, May, 2017, pp. 1665–1677.
- [20] L. Sigríst, I. Egido, E. L. Miguélez, L. Rouco, "Sizing and controller settling of ultracapacitors for frequency stability enhancement of small isolated power systems," in *IEEE Transactions on Power System*, vol.30, no.4, July, 2015, pp.2130–2138.
- [21] T. Kerdphol, F. S. Rahman, Y. Mitani, "Virtual Inertia Control Application to enhance frequency stability of interconnected power systems with high renewable energy penetration," in *Energies Journal*, vol. 11, no. 4, 2018, pp. 981–997.
- [22] X. Zhang, F. Mao, H. Xu, F. Liu, M. Li, "An Optimal Coordination Control Strategy of Micro-Grid Inverter and Energy Storage Based on Variable Virtual Inertia and Damping of VSG," in *Chinese Journal of Electrical Engineering*, December 2017, pp. 25–33.
- [23] J. Liu, Y. Miura, T. Ise, "Comparison of dynamic characteristics between virtual synchronous generator and droop control in inverter-based distributed generators," in *IEEE Transaction on Power Electronics*. Vol 31, pp. 3600–3611.

- [24] H.P.Beck, R. Hesse, “Virtual synchronous machine,” in *Proceedings of the 9th International Conference on Power Quality and Utilizations*, Barcelona, Spain, October 2007, pp. 1–6.
- [25] V. Karapanos, S. Haan, K. Zwetsloot, “Real time simulation of a power system with VSG hardware in the loop,” in *Proceedings of the 37th Annual conference on IEEE Industrial Electronics Society*, Melbourne, Australia, November 2011, pp. 3748–3754.
- [26] Q.C. Zhong, G. Weis, “Synchroverter: Inverters that mimic synchronous generators,” in *IEEE Transaction on Industrial Electronics*, 2011, pp. 1259–1265.
- [27] J. Cao, W. Du, H. Wang, M. McCulloch, “Optimal Sizing and Control Strategies for Hybrid Storage System as Limited by Grid Frequency Deviations,” in *IEEE Transactions on Power system*, vol. 33, no. 5, September, 2018, pp. 5486–5495.
- [28] J. Alipoor, Y. Miura, T. Ise, “Power system stabilization using virtual synchronous generator with alternating moment of inertia,” *IEEE Emerging and Selected Topics in Power Electronics*, vol.3, no.2, pp.451–458, 2014.
- [29] M. A. Torres, L. A. C. Lopes, L. A. Morán, J. R. Espinoza, “Self-tuning virtual synchronous machine: A control strategy for energy storage systems to support dynamic frequency control,” in *IEEE Transaction on Energy Conversion*, vol. 29, no. 4, December, 2014, pp. 833–840.
- [30] Z.P. Lv, W.X Sheng, Q.C ZHONG, et al, “Virtual Synchronous Generator and Its Applications in Micro-grid,” in *Proceedings of the CSEE*, vol 34, no 16, pp 2591–2603, June, 2014.
- [31] X. Zhan, D. B. Zhu, H. Z. Xu, “Technology of Virtual Synchronous Generator in Distributed Generation,” in *Actaines of Electrical Engineering*, vol. 10, no. 3, pp 1–6, May 2012.
- [32] R.H.L.C. Hochgraf, D.M. Divan, T.A. Lipo, “Comparison of multilevel Inverters for Static Var Compensation,” *Wisconsin Power Electronics Center*, University of Wisconsin-Madison, 1994.
- [33] C.L. Moreira, F.O. Resende, and J.A.P. Lopes, “Using Low Voltage MicroGrids for Service Restoration,” in *IEEE Transactions on Power System*, vol. 22, pp. 395–403, 2007.
- [34] J.A.P. Lopes, C.L. Moreira, F.O. Resende, “Microgrids black start and islanded operation,” in *15th PSCC*, Liege, 2005.
- [35] J.A.P. Lopes, C.L. Moreira, and A.G. Madureira, “Defining control strategies for MicroGrids islanded operation,” in *IEEE Transactions on Power System*, vol. 21, pp. 916–924, 2006.
- [36] J. Pou, M.A. Perez, R.P. Aguilera, “Modular Multilevels Converters,” in *IEEE Transactions on Industrial Electronics*, vol. 66, no. 3, pp. 2204–2206, March, 2019.
- [37] Y. Luo, Z. Li, Y. Li, P. Wang “A Distributed Control Method for Power Module Voltage Balancing of Modular Multilevel Converters,” in *Proceedings of the 2016 IEEE Energy Conversion Congress and Exposition*, (ECCE), September, 2016.

- [38] C. Pineda, J. Pereda, X. Zhang, F. Rojas, “Triangular Current Mode for High Step Ratio Modular Multilevel dc-dc Converter,” in *Proceedings of the 2018 IEEE Energy Conversion Congress and Exposition*, (ECCE), pp. 5185–5189, September, 2018.
- [39] S. Debnath, J. Qin, B. Bahrani, M. Saeedifard, P. Barbosa, “Operation, Control, and Applications of the Modular Multilevel Converter: A Review,” in *IEEE Transactions on Power Electronics*, vol. 30, no. 1, pp. 37–53, January, 2015.
- [40] B. Li, M. Guan, D. Xu, R. Li, G.P. Adam, B. Williams, “A Series HVDC Power Tap Using Modular Multilevel Converters,” in *Proceedings of the 2016 IEEE Energy Conversion Congress and Exposition*, (ECCE), September, 2016.
- [41] A.O. Almeida, F.T. Ghetti, A.S.B. Ribeiro, P.M. Almeida, P.G. Barbosa, “Circulating Currents Suppression Strategies for Modular Multilevel Converter,” in *Proceedings of Brazilian Power Electronics Conference*, (COBEP), November, 2017.
- [42] F. Qin, F. Gao, T. Xu, D. Niu, Z. Ma, “A Control Scheme of Nine-Arm Modular Multilevel Converter,” in *Proceedings of 2018 IEEE Energy Conversion Congress and Exposition*, (ECCE), September, 2018.
- [43] J. Qin, M. Saeedifard, “Predictive Control of a Modular Multilevel Converter for a Back-to-Back HVDC System,” in *IEEE Transactions on Power Delivery*, vol.27, pp.1538–1547, 2012.
- [44] M. A Parker, L. Ran, S. J. Finney, “Distributed Control of a Fault Tolerant Modular Multilevel Inverter for Direct-Drive Wind Turbine Grid Interfacing,” in *IEEE Transactions on Industrial Electronics*, vol. 60, pp. 509–522, 2013.
- [45] H. Ji, A. Chen, Q. Liu, C. Zhang, “A New Circulating Current Suppressing Control Strategy for Modular Multilevel Converters,” in *Proceedings of the 36th Chinese Control Conference*, July, 2017.
- [46] P. M. Prafullachandra, V. B. Borghate, “A Simplified Nearest Level Control (NLC) Voltage Balancing Method for Modular Multilevel Converter (MMC),” in *IEEE Transaction on Power Electronics*, vol. 30, no. 1, January, 2015.
- [47] M. Saeedifard, R. Iravani, “Dynamic performance of a modular multilevel back-to-back HVDC system,” in *IEEE Transactions on Power Delivery*, vol. 25, no. 4, pp. 2903–2912, October, 2010.
- [48] Z. Liu, Z.-x. Liu, C. Li, C. Fu, “Improved voltage balancing method base don MMC nearest level modulation,” in *Proceedings of the 36th IEEE Control Conference (CCC)*, 2017, PP. 10359–10364.
- [49] H. Saad, Y. Fillion, S. Deschanvres, Y Vernay, S. Dennetière, “Hardware realization and analysis of a seven level reduced switch inverter with space vector modulation technique,” in *2017 Second International Conference on Electrical, Computer and Communication Technologies (ICECCT)*, India, 2017.
- [50] A. J. Marin-Hurtado, W. J. Gil-Gonzalez, A. Escobar-Mejía, C. Deng, “Comparison PIR and MPC Control Scheme to Reduce Circulating Current in a Modular Multilevel Converter Terminal,” in *Proceedings 2019 IEEE Energy Conversion Congress and Exposition* (ECCE), United States, November, 2019.

- [51] M. Hagiwara, H. Akagi, "Control and Experiment of pulse width-modulated modular multilevel converters," in *IEEE Transactions on Power Electronics*, vol. 24, no. 7, 2009, pp.1737–1746.
- [52] M. Hagiwara, R. Maeda, H. Akagi, "Control and analysis of the modular multilevel cascade converter based on double-star chopper-cells (mmcc-dscc)," in *IEEE Transactions on Power Electronics*, vol. 26, no. 6, pp. 1649–1658, 2011.
- [53] D.A. Guzman Pinzon, "High voltage direct current energy transmission using modular multilevel converters," Master of Science in Electrical Engineering, University of Arkansas, 2013.
- [54] P. Kundur, "Power System Stability and Control," New York, US, McGraw-Hill.
- [55] C. Zhang, Y. Yang, H. Miao, X. Yuan, "An Improved Adaptive Inertia and Damping Control Strategy for Virtual Synchronous Generator," in *Proceedings 2018 13th IEEE Conference on Industrial Applications (ICIEA)*, Wuhan, May, 2018.
- [56] Z. LV, Q. Chang-Zhong, "Control of modular multilevel converters as virtual synchronous machines," in *Proceedings 2017 IEEE Power & Energy Society General Meeting*, Chicago, July, 2017.
- [57] A.E. Fitzgerald, C. Kingsley, S.D. Umans, "Electric Machinery," New York, Us, second edition, McGraw-Hill, 2003.
- [58] Q. Chang-Zhong, "Synchronverters: Inverters That Mimic Synchronous Generators," in *IEEE Transactions on Industrial Electronics*, vol. 50, no. 4, pp. 1259–1267, April, 2011.
- [59] A. Perera, "Virtual Synchronous Machine-based Power Control in Active Rectifiers for Micro Grids", Msc thesis, Department of Electric Power Engineering, Norwegian University of Science and Technology, Noruega.
- [60] H. Bevrani, "Virtual Inertia-Based Frequency Control," in *Robust Power System Frequency Control*, J.J. Chow, A.M. Stankovic, D. Hill, Second Edition, Switzerland, Springer, 2014, pp. 349–374.
- [61] F. Bignucolo, R. Stecca, M. Coppo, "Advantages of the Virtual Synchronous Machine regulation for integrating Low-Inertia Variable Renewable Generation in Transmission Systems," in *Proceedings of the 53rd International Universities Power Engineering Conference (UPEC)*, Glasgow, UK, 2018.
- [62] Q. Zhong, "Virtual Synchronous Machine: A unified interface for grid integration," in *IEEE Power Electronics Magazine*, vol.3, no. 4, pp. 18–27, December, 2016.
- [63] S. D'Arco, J. A. Suul, "Virtual Synchronous Machine-Classification of implementation and analysis of equivalence to droop controllers for microgrids," in *Proceedings of the 2013 Grenoble Conference*, pp. 1–7, Grenoble, France, June, 2013.
- [64] M. P. N. V. Wesenbeeck, S. H. W. de Hann, P. Varela, K. Visscher, "Grid tied converter with virtual kinetic storage," in *Proceedings of the 2009 Bucharest Power Tech*, Bucharest, Romania, October, 2009.
- [65] E. U. Ruiz, "Control and Stability of AC/DC Microgrids," Doctoral Thesis, Electronics and Computing Department, Mondragon Unibertsitatea, Arrasate, 2017.

- [66] K. Koyanagi, Y. Hida, Y. Ito, K. Yoshimi, R. Yokoyama, M. Inokuchi, T. Mouri, and J. Eguchi, "A Smart Photovoltaic Generation System Integrated with Lithium-ion Capacitor Storage," in *Proceedings of the 2011 46th International Universities' Power Engineering Conference (UPEC)*, Soest, Germany, pp. 1–6, September, 2011.
- [67] O. Mo, S. D'Arco, J. A. Suul, "Evaluation of Virtual Synchronous Machines with Dynamic or Quasi-Stationary Machine Models," in *IEEE Transactions on Industrial Electronics*, vol. 64, no. 7, pp. 5952–5962, July, 2017
- [68] Q. Zhong, P. Nguyen, Z. Ma, W. Sheng, "Self-Synchronized Synchronverters: Inverters Without a Dedicated Synchronization Unit," in *IEEE Transactions on Power Electronics*, vol. 29, no. 2, pp. 617–630, February, 2014.
- [69] H. Lao, L. Zhang, T. Zhao, L. Zou, "Frequency regulation strategy for DFIG combining over-speed control and adaptive virtual inertia," in *Proceedings 2019 IEEE Innovative Smart Grid Technologies-Asia (ISGT Asia)*. IEEE, 2019, pp.1663–1666.
- [70] U. Markovic, Z. Chu, P. Aristidou, G Hug, "LQR-Based Adaptive Virtual Synchronous Machine for Power Systems with High Inverter Penetration," in *IEEE Transactions on Sustainable Energy*, vol. 19, no. 3, pp. 1501–1512, July, 2019.
- [71] L. Wang, "Discrete-time MPC for Beginners," in *Model Predictive Control System Design and Implementation Using MATLAB*, Melbourne, Australia, 2009, pp. 1–39.